UNIVERSIDAD DE INVESTIGACIÓN DE TECNOLOGÍA EXPERIMENTAL YACHAY

Escuela de Ciencias Físicas y Nanotecnología

TÍTULO: Spectroscopic and Microscopic Characterization of Homogeneous Dispersed Kaolinite/Carbon Nanotubes Nanocomposites

Trabajo de integración curricular presentado como requisito para la obtención
del título de Ingeniero en Nanotecnología

Autor:

Hinojosa Chasiquiza Vanessa G.

Tutor:

Dr. rer. nat. Chacón Torres Julio C

Urcuquí, agosto 2019

Urcuquí, 22 de agosto de 2019

SECRETARÍA GENERAL
(Vicerrectorado Académico/Cancillería)
ESCUELA DE CIENCIAS FÍSICAS Y NANOTECNOLOGÍA
CARRERA DE NANOTECNOLOGÍA
ACTA DE DEFENSA No. UITEY-PHY-2019-00012-AD

En la ciudad de San Miguel de Urcuquí, Provincia de Imbabura, a los 22 días del mes de agosto de 2019, a las 08:30 horas, en el Aula Sala Capitular de la Universidad de Investigación de Tecnología Experimental Yachay y ante el Tribunal Calificador, integrado por los docentes:

Presidente Tribunal de Defensa	Dra. BRICEÑO ARAUJO, SARAH ELISA , Ph.D.
Miembro No Tutor	Dr. LOBOS MARTIN, JUAN , Ph.D.
Tutor	Dr. CHACON TORRES, JULIO CESAR , Ph.D.

Se presenta el(la) señor(ita) estudiante HINOJOSA CHASIQUIZA, VANESSA GISELLE, con cédula de identidad No. 0503428385, de la ESCUELA DE CIENCIAS FÍSICAS Y NANOTECNOLOGÍA, de la Carrera de NANOTECNOLOGÍA, aprobada por el Consejo de Educación Superior (CES), mediante Resolución RPC-SO-13-No.156-2015, con el objeto de rendir la sustentación de su trabajo de titulación denominado: Spectroscopic and Microscopic Characterization of Homogeneous Dispersed Kaolinite/Carbon Nanotubes Nanocomposites, previa a la obtención del título de INGENIERO/A EN NANOTECNOLOGÍA.

El citado trabajo de titulación, fue debidamente aprobado por el(los) docente(s):

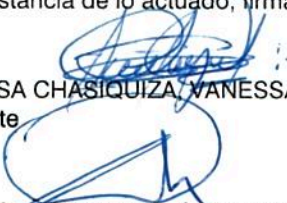|	
Tutor	Dr. CHACON TORRES, JULIO CESAR , Ph.D.

Y recibió las observaciones de los otros miembros del Tribunal Calificador, las mismas que han sido incorporadas por el(la) estudiante.

Previamente cumplidos los requisitos legales y reglamentarios, el trabajo de titulación fue sustentado por el(la) estudiante y examinado por los miembros del Tribunal Calificador. Escuchada la sustentación del trabajo de titulación, que integró la exposición de el(la) estudiante sobre el contenido de la misma y las preguntas formuladas por los miembros del Tribunal, se califica la sustentación del trabajo de titulación con las siguientes calificaciones:

Tipo	Docente	Calificación
Presidente Tribunal De Defensa	Dra. BRICEÑO ARAUJO, SARAH ELISA , Ph.D.	10,0
Miembro Tribunal De Defensa	Dr. LOBOS MARTIN, JUAN , Ph.D.	9,4
Tutor	Dr. CHACON TORRES, JULIO CESAR , Ph.D.	10,0

Lo que da un promedio de: 9.7 (Nueve punto Siete), sobre 10 (diez), equivalente a: APROBADO

Para constancia de lo actuado, firman los miembros del Tribunal Calificador, el/la estudiante y el/la secretario ad-hoc.
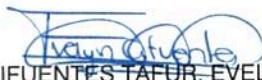
HINOJOSA CHASIQUIZA, VANESSA GISELLE
Estudiante

Dra. BRICEÑO ARAUJO, SARAH ELISA , Ph.D.
Presidente Tribunal de Defensa

Dr. CHACON TORRES, JULIO CESAR , Ph.D.
Tutor

Dr. LOBOS MARTIN, JUAN , Ph.D.
Miembro No Tutor

CIFUENTES TAFUR, EVELYN CAROLINA
Secretario Ad-hoc

Autoría

Yo, **VANESSA GISELLE HINOJOSA CHASIQUIZA**, con cédula de identidad 0503428385, declaro que las ideas, juicios, valoraciones, interpretaciones, consultas bibliográficas, definiciones y conceptualizaciones expuestas en el presente trabajo; así cómo, los procedimientos y herramientas utilizadas en la investigación, son de absoluta responsabilidad de el/la autora (a) del trabajo de integración curricular. Así mismo, me acojo a los reglamentos internos de la Universidad de Investigación de Tecnología Experimental Yachay.

Urcuquí agosto 2019.

VANESSA GISELLE HINOJOSA CHASIQUIZA

CI:0503428385

Autorización de publicación

Yo, **VANESSA GISELLE HINOJOSA CHASIQUIZA**, con cédula de identidad 0503428385, cedo a la Universidad de Tecnología Experimental Yachay, los derechos de publicación de la presente obra, sin que deba haber un reconocimiento económico por este concepto. Declaro además que el texto del presente trabajo de titulación no podrá ser cedido a ninguna empresa editorial para su publicación u otros fines, sin contar previamente con la autorización escrita de la Universidad.

Asimismo, autorizo a la Universidad que realice la digitalización y publicación de este trabajo de integración curricular en el repositorio virtual, de conformidad a lo dispuesto en el Art. 144 de la Ley Orgánica de Educación Superior

Urcuquí, agosto 2019.

VANESSA GISELLE HINOJOSA CHASIQUIZA

CI:0503428385

Acknowledgements

I would like to express my gratitude to my supervisor, Dr. Julio C. Torres-Chacón for his endless patience and help throughout this project. His support, outstanding knowledge of the subject and incomparable professionalism allowed me to develop an enjoyable and truly informative experience.

I would like to thank the members of my committee for taking the time to consider my thesis and partake in my defense.

Especially, I would like to thanks to my mother Jenny Chasiquiza who always support me and avoid that I give up. My father Patricio Hinojosa who teach me to be on calm in stress situation and thinking objectively. My sister Alison Hinojosa from who I learn to be strong although the situations exceed my capacities. I would like to thank all my family, grandparents, uncles, aunts, cousins who always care about me.

Finally, I would like to mention my friends Byron Tipán (Franky), Cristhian Proaño, Cristian Chingo, Lorena Layana which support me, teach me, listen me, and being my friends. Especially to my boyfriend Kabir Sulca because the life is sweet with you.

Resumen

En los últimos años, los nanotubos de carbono han generado un gran interés en el campo de la Nanotecnología debido a sus extraordinarias propiedades electrónicas y mecánicas[1]. Existen muchos tipos de investigación en los que los nanocompuestos se desarrollan utilizando nanotubos de carbono para mejorar las propiedades de un determinado material[2]. Un material para mejorar sus propiedades podría ser la arcilla caolinita, que posee alta conductividad térmica, alta capacidad de intercambio de cationes y una gran área de superficie[3,4] y se ha utilizado ampliamente en la industria de la pintura, la vivienda y el petróleo[5]. En este trabajo, se sintetizaron nanocompuestos basados en arcilla de caolinita y nanotubos de pared múltiple (MWCNTs). Se produjeron cuatro tipos de nanocompuestos con diferentes concentraciones de MWCNTs. La cantidad de MWCNTs en los nanocompuestos fue 5, 1, 0.1 y 0.05 % de peso en relación de peso de caolinita. Los nanocompuestos se caracterizaron por espectroscopía Raman y Scanning Electron Microscopy (SEM). El espectro Raman de los nanotubos pristine presentó las bandas características: la banda D alrededor de 1339 cm^{-1}, la banda G^{+} alrededor de 1570cm^{-1}, la banda G^{-} alrededor de 1595 cm^{-1}, y la banda G' alrededor de 2670 cm^{-1}. Los cambios en el espectro Raman de los nanocompuestos suguirieron transferencia de carga, dopaje, formación de carbono amorfo e hibridación sp^{3}. Dos nuevos picos alrededor de 1446 cm^{-1} y 1542 cm^{-1} aparecieron en los nanocompuestos con la concentraci'on de 1, 0.1 y 0.05 wt. % de nanotubos de carbono asignados a la formación de carbono amorfo e hibridación sp^{3} respectivamente. En los nanocompuestos con la concentración más baja de MWCNTs apareció un tercer pico nuevo a 1160 cm^{-1} que se asoció con una formación de fase con alto contenido de hibridación sp^{3} en los nanocompuestos . Las imágenes SEM permitieron medir el tamaño de grano de la arcilla de caolinita y el diámetro de los nanotubos de carbono.

Palabras clave: Nanotubos de carbono, caolinita, espectroscopía Raman, nanocompuestos

Abstract

In recent years, carbon nanotubes have generated a lot of interest in the Nanotechnology field due to their extraordinarily electronic and mechanical properties[1]. There exist several types of research in which nanocomposites are developed using carbon nanotubes to enhance the properties of a certain material[2]. One material to enhance its properties could be Kaolinite clay which posses high aspect ratio, high thermal conductivity, high cation exchange capacity, and large surface area[3,4] and it has been widely used in paint, housing, and petroleum industry[5]. In this work, nanocomposites based on Kaolinite clay and Multiwalled Carbon Nanotubes (MWCNTs) were synthesized: Kaolinite/MWCNT nanocomposites (Kaol-MW nanocomposites). It was produced four types of nanocomposites with different concentrations of MWCNTs. The quantity of MWCNTs in the nanocomposites was 5, 1, 0.1, and 0.05 by wt.%. of Kaolinite. The nanocomposites were characterized by Raman spectroscopy and Scanning Electron Microscopy (SEM). The Raman spectrum of the pristine MWCNTs presented the characteristic bands: the D band around 1339 cm^{-1}, the G^+ band around 1570 cm^{-1}, the G^- band around 1595 cm^{-1}, and the G' band around 2670 cm^{-1}. The changes in the Raman spectrum of the nanocomposites advised charge transfer, doping, the formation of amorphous carbon and sp^3 hybridization. Two new peaks around 1446 cm^{-1} and 1542 cm^{-1} appeared in the nanocomposites with the concentration of MWCNTs of 1, 0.1, and 0.05 wt.% assigned to the formation of amorphous carbon and sp^3 hybridization respectively. In the nanocomposites with the lowest concentration of MWCNTs a third new peak appeared at 1160 cm^{-1} that was associated with a stage phase formation with high sp^3 hybridization content in the nanocomposites. SEM images allowed to measure the grain size of the kaolinite clay and carbon nanotubes diameter.

Keywords: Carbon Nanotubes, Kaolinite, Raman spectroscopy, Nanocomposites

Contents

List of Figures

List of Tables

List of Presentations

[1] Characterization of a Homogeneous Dispersed Kaolinite/Carbon Nanotubes Nanocomposites in the Nanoscience Summer School Yachay 2019

Chapter 1

Introduction

Nanoscience and Nanotechnology are based on the manipulation of molecules and individual atoms to produce materials from them with a tiny size called nanomaterials[6]. It is not just the production of nanomaterials, but also the introduction of them into larger systems and incorporates them in the real world[6]. In this way, there exist many possibilities for consumer applications exist as a result of the advancements in the field of Nanotechnology[7]. According to the National Nanotechnology Initiative (NNI) in the United State "nanotechnology is the understanding and control of matter at dimensions between approximately 1 and 100 nanometers, where unique phenomena enable novel application"[6]. These unique phenomena that NNI mentions it is referred to the fact that the nanoscale is different from the macro scale which makes the nano-world so interesting[6]. One hand, in materials with a size of microns and above called bulk materials, their properties follow the rules of Newtonian physics. On the other hand, in submicroscopic objects whose dimensions are between 1 μm and 100 nm, their properties are affected by fluctuations and become subject to the strange and unpredictable laws of quantum mechanics[6]. For instance, as the length scale decreases in material there is an increasing percentage of the number of atoms that are situated on the surface of the objects which is called the surface area[7]. Furthermore, it is possible to control the fundamental properties of materials such as their melting temperature, magnetic properties, charge capacity, and even their color without changing the materials' chemical compositions by creating nanomaterials[8]. Among of the thousand nanomaterials that exist, Carbon Nanotubes (CNTs) have been widely used to combine them with other materials due to their structural, electrical, and mechanical properties which made them an ideal reinforcement for a variety of materials including polymers, metal/alloys, and ceramics[9].

Since CNTs were reported at the first time in 1952 by Radushkevich *et al* in Russian, then by Endo *et al* in 1972[10], and finally reported in English by Iijima in 1991, they have brought a lot of interest in the scientific community due to their unique properties which promise unimaginable applications[11]. Among the most outstanding properties are their extraordinary mechanical strength, nanometer size, high aspect ratio (the proportional relationship between its width and its height), exceptionally high electrical and thermal conductivity, display devices, quantum computing and composite materials[2,12]. In the same way, the effort for characterizing the CNTs structure and to determine their physical properties has been stimulated extensively since their discovery[13]. CNTs can be classified into three types:

Single-walled Carbon Nanotube (SWCNT), Multiwalled Carbon Nanotube (MWCNT), and other types of CNTs such as extreme carbon nanotubes, torus, nanobud, pea pod, and cup-stacked CNTs[14]; in this work just SWCNTs and MWCNTs will be discussed and we worked with MWCNTs. SWCNTs consists of just one wrapped graphene sheet while MWCNTs is a collection of concentric SWCNTs, but their diameter and properties are different[15]. A lot of theoretical and experimental research has demonstrated the sizable properties of CNTs for use as super strong fibers, composites, catalysts, molecular straws, and even as molecular switches[16]. There exist several types of research in which CNTs was used as reinforcement material and was combined with other materials to enhance their properties[2]. In the same way that CNTs have been reported as good reinforcement material, clays have been reported as a good matrix material for anchoring[17].

Clays are interesting materials which have applications in the various process such as industries engineering, petroleum discovery, recovery and refining, all of them attributed to their structure and composition[5]. The important characteristics of clays for the mentioned applications are the particle size and shape, surface chemistry, surface area, and other physical and chemical properties specific to a particular application such as viscosity, plasticity, color, green, absorption and adsorption, dry and fired strength, abrasion, and others[5]. One way to classify clays is based in their layered structure[18]. Kaolin is a group of dioctahedral 1:1 layer silicates which consist in two-layered material formed by one tetrahedral and one octahedral cation sheet linked by bridging oxygen atoms. Kaolin includes kaolinite, halloysite, dicktite, and nacrite clay minerals[19]. In this work, we will focus in Kaolinite clay (Kaol) which is the most important clay mineral with high aspect ratio, high thermal conductivity, high cation exchange capacities, and large surface area[3,19,20]. Kaol is an abundant mineral clay in nature with a hardness about 1.5 in the Mosh scale, the chemical formula is $Al_2Si_2O_5(OH)_4$, and it is chemically inert[5,18]. The layered structure of Kaol has been used to polymerize into its layered structure. Kaol has been reported as a good matrix material for anchoring in nanocomposites with TiO_2 and silver nanoparticles[17,21]. The space between layers may be expanded to the size necessary for nanoparticle synthesis by breaking up the hydrogen bonds tightly interlinking the kaolinite lamellae[17]. Furthermore, Kaol has been extensively studied and nanocomposites based on it have been developed especially to waste treatment and pollution[22]. A piece of detailed information about the structure and properties of CNTs will be presented in Chapter 2.

Nanocomposites are innovative materials that have became the materials of the 21st century in the view of possessing uniqueness and property combinations that are not found in conventional composites[23,24]. The field of nanocomposites involves the study of multiphase materials with at least one phase constituent in the nanoscale (less than 100 nm)[25]. Nanocomposites are materials that incorporate nanosized particles into a matrix of a standard material and can be considered as solid structures with repeat distances between the different phases that constitute the structure[25]. They have gained a lot of interest in scientist and engineers in the recent years as a result of the possibility to design and create new materials with unprecedented flexibility and improvements in their physical properties using nanosize building blocks[25]. In several interdisciplinary fields, it has been demonstrated the ability to tailor composites by using nanosize building blocks of heterogeneous chemical species[25]. Nanocomposites serve various functions because their constituents usually have different structure and composition and hence different properties[25]. The importance of producing nanocomposites is the fact that they offer useful new properties compared with conventional materials[25]. The nanomaterials that are added to improve a standard material are very effective in

such a way that normally the amount of nanomaterials used is only between 0.5 and 5% by weight[26]. The main factor in nanocomposites is their extremely high surface to volume ratio which can dramatically change their properties in comparison with the bulk material[26]. In some cases, the nanocomposites achieved to be 1000 times tougher than the bulk component[26]. Okpala[8] reported some property enhancements that nanomaterial additives can provide in comparison to both their conventional filler counterparts and base polymer:

- Mechanical properties e.g. strength, modulus, and dimensional stability

- Decreased permeability to gases, water, and hydrocarbons

- Thermal stability and heat distortion temperature

- Flame retardancy and reduced smoke emissions

- Chemical resistance

- Surface appearance

- Electrical conductivity

- Optical clarity in comparison to conventionally filled polymers

- Others: improvement in modulus, flexural strength, heat distortion temperature, barrier properties,

CNTs and clays have been used to prepare nanocomposites with outstanding properties and applications. Song[27] reported nanocomposites made of modified MWCNTs and montmorillonite (clay) to integrate it into elastomer composites improving mechanical, thermal and electrical properties of the elastomer composites. Oil split remediation could be done with nanosponges of modified montmorillonite nanocomposites as it was reported by Sedaghat[28]. CNTs rooted in smectite clays was reported as hybrid material to introduce them into a membrane in order to enhance proton transport properties[29]. Furthermore, kaolinite was used to grow vertically aligned CNTs obtaining an enlargement of the overgrown humps and an increase in their areal density[30]. Detail information of nanocomposites based on kaolinite and CNTs is developed in the Chapter 2.

In order to understand the characteristics of nanomaterials and composites based on them, it is needed to analyze then trough characterization techniques. Valcárcel[31] define characterization as "the action for establishing the differential aspects of an object or system on the basis of analytical results"[31]. In the present work, characterization techniques are considered as tools which give information about the structure and electronic properties of the material to be analyzed. Two characterization techniques were employed: microscopic and spectroscopic techniques. Scanning Electron Microscopy (SEM) is a microscopic technique that allows direct observation of size, shape, and morphology[15,32] of nanomaterials with a better resolution than light microscope which could provide images of 1-20 nm resolution. It uses an electron beam which interacts with atoms and produces images, it is commonly used to analyze morphology and length in CNTs[15]. Among of spectroscopic techniques to characterize CNTs, Raman spectroscopy has been one of the most powerful technique to characterize not just CNTs, but also carbon materials[1]. It uses visible light which interacts inelastically with the sample and it returns to a detector with higher or lower

energy, and it could give structural, vibrational and electronic information of CNTs[1,33]. The complete description of the characterization techniques used in this work is presented in Chapter 2.

Although nanocomposites based on carbon nanotubes and its characteristics have been widely studied, there are very few studies that report nanocomposites of Kaol with carbon nanotubes as reinforcement material[34]. The majority of Kaol and CNTs nanocomposites are focused on the growth of nanotubes using Kaol or other clay as a substrate or a catalyst. A detailed analysis of the results of the characterization techniques has not been found especially in the Raman results which are the ones that provide the most information. Chapter 3 contains the aspects that motivate us to study nanocomposites of Kaol and MWCNTs. With this in mind, the objective of this work is preparing nanocomposites made of Kaol and MWCNTs, and it is of interest to find the optimal concentration of MWCNTs in the nanocomposites which were achieved preparing nanocomposites with different concentrations of MWCNTs and analyzing them through Raman and SEM characterization. The detailed nanocomposites preparation is described in the Chapter 4. Additionally, it is our aim to provide relevant information of doping, charge transfer, crystallinity, and hybridization of nanocomposites made out of MWCNTs as a reinforcement material and Kaol as the matrix material. These characteristics can be described by the detailed analysis of their the Raman spectrum of the nanocomposites compared with the pristine material and using SEM images to analyze the nanocomposites morphology, grain size and distribution. The complete Raman and SEM analysis is shown in the Chapter 5. Finally, these results could be used as a basis for future mechanical tests of the nanocomposites that have shown an interaction between its components. It is developed in the Chapter 6

Chapter 2

Theoretical Principles

In this chapter, an overview of the structure of Carbon Nanotubes (CNTs) and Kaolinite clay (Kaol) will be presented along to their composition and properties. It contains a review of research information about these materials and nanocomposites made with them.

2.1 Carbon allotropes

Carbon is the basic element for life and organic chemistry[35,36]. Carbon has the capacity to combine with itself and other organic compounds, giving rise to a rich diversity of structural forms of carbon with different properties each one[35,36]. This capability to form different structures is called allotropy. In general, molecular orbitals bound with the same kind of orbitals which means that a s orbital will bind with another s orbital or a p orbital with a p orbital[37]. In the case of C, the bonding is not necessary with the same kind of orbital, and it is possible to mix molecular orbitals[37]. The electronic configuration of C in the ground state is $(1s^2)(2s^2)(2p^2)$ which means that the outer shell has two unpaired electrons that could make only two bonds[37]. Experimental results have shown that it is possible to have four bonds in a C atom like in methane[37]. It occurs due to the small difference in energy of $2s$ and $2p$ state which implies that electrons from $2s$ state can be excited easily to the $2p$ state with an external perturbation such as the presence of hydrogen[37]. It produces mixed states as it is shown in Fig. 2.1, an sp^3 orbital is produced between three p states with one s state (Fig. 2.1a), sp^2 appears when two p states are combined with one s state (Fig. 2.1b), and just one p state with one s state form the sp^1 orbital (Fig. 2.1c)[37]. Each one has different structures, electron geometry, and properties. The sp^3 hybridization forms a tetrahedral assembly with 109.5 degrees between each orbital resulting in very strong bounds like in diamond[37]. The sp^2 hybridization produces a planar assembly with 120 degrees of separation of each hybrid orbital which could make σ bonds, and a π orbital with is responsible for Van der Waals forces like in graphite. Finally, the sp^1 hybridization has a linear geometry with 180 degrees between the new orbitals.

(a) sp^3 (b) sp^2 (c) sp^1
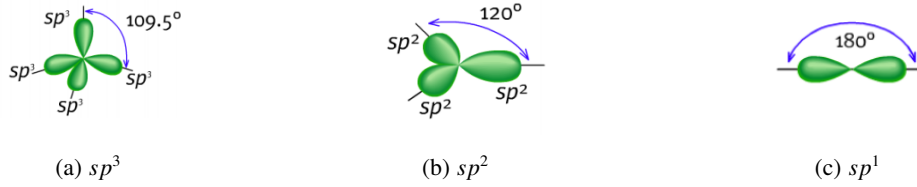
Figure 2.1: Hybrid molecular orbitals of carbon (source: Peschel, 2011)

Some of the most studied and stable forms of carbon are diamond, graphite, graphene, fullerenes, and carbon nanotubes. Diamond is the hardest material known which presents a 3D structure with a transparent appearance[37]. It is a solid form of C and frequently found in a cubic form[36]. C atoms are ordered in a tetrahedral form via sp^3 hybridization in which the σ bond between neighbors gives to diamond the binding strength[36]. Diamond has high thermal conductivity and melting temperature, a band gap of 5 eV that corresponds to an insulator, and its electrical conductivity are very low[36,38]. The transparent appearance of diamond derives from the fact that the electrons in the valence band cannot be excited to the conduction band with a wavelength in the optical range[37]. In contrast, graphite is a soft and opaque crystal made of layers of C in a hexagonal arrangement. This structure can be formed when C atoms present sp^2 hybridization[37] . Each sp^2 orbital is combined with other three sp^2 orbitals in a σ bond forming a hexagonal planar pattern. The π orbital corresponds to the free delocalized electron and is oriented perpendicular to the plane made of sp^2 orbitals[36]. Each layer has one delocalized electron, and they are bonded together through Van der Waals forces and they are stacked in the z-direction with an interlayer spacing of 0.332 nm[36,39]. The gray appearance of graphite is due to the radiation in the visible range that excites electrons from the valence band to the conduction band[37]. If graphite splits into more tin sheets repeatedly via the scotch tape method which is a mechanical exfoliation[40], the resulting structure will be called graphene[2,14]. Graphene is a carbon allotrope that consists of a single layer of C atoms ordered in a hexagonal lattice[2,14,36]. It is the basic building block of other carbon allotropes like fullerenes or carbon nanotubes. The mobility of electrons at room temperature in graphene arise high values which are as high as 15000 cm^{2}V^{1}s^1. Fig. 2.2 shows the unit cell and the reciprocal space of graphene where $\vec{a_1}$ and $\vec{a_2}$ are the vectors that describe the unit cell and $\vec{b_1}$, $\vec{b_2}$ are the vectors in the reciprocal space. The shadow region represents the First Brillouin Zone (FBZ) with the characteristic symmetric points
Gamma, K, and M. In the reciprocal space, Γ is the point where the momentum state $(\vec{k}) = \vec{0}$. At the midpoint of the boundary segment of the FBZ the M point, $\vec{k} = \frac{2\pi}{a_0} \sqrt{3}\hat{k}_y$. The K and K' points are located at $|\vec{k}| = \frac{4\pi}{a_0}$ 2

(a) unit cell   (b) reciprocal space

Figure 2.2: a) Honeycomb lattice of graphene with the unit vectors a_1 and a_2 in the real space, and b) reciprocal space of graphene with vectors b_1 and b_2 an the symmetric points Γ, K, M, and M' (based on Dresselhaus *et al.*, 2005)

Another allotropes of C are fullerenes, atoms in the fullerenes are ordered in a spherical network like a football where the atoms have a sp^2 hybridization, and the smallest stable and most prominent is C_{60}[35]. It is formed by pentagons and hexagons and it is needed exactly twelve pentagons in the structure to close the shape[42]. The hybridization of fullerenes is a little more complicated than other allotropes, it is a modification of the sp^3 and sp^2 orbital[42]. The σ orbital does not contain all character of the s orbital and the π orbital does not contain all the p-orbital character. Also, the hybridization is not fixed, it depends on the number of atoms in the molecule. It is edgeless, chargeless, and it has no boundaries, no dangling bonds, and no unpaired electrons[42]. Finally, CNTs belongs to the family of fullerenes whose name comes from its cylindrical structure[14]. It is a one-dimensional structure of one atom thickness consisting in a wrapped monolayer graphene sheet in a seamless way to a cylinder[41,43,44]. It will be described in detail in the following section.

2.2 Carbon Nanotubes

CNTs have been widely studied as well as their structure, properties, and applications. Despite to be well documented, scientists are still finding new properties of them[44]. There is two principal types of CNT: Single-walled Carbon Nanotube (SWCNT) Multiwalled Carbon Nanotube (MWCNT)[15]. Other kind of CNTs like G' carbon nanotubes, extreme carbon nanotubes, and pea pod are in the category of other carbon nanotubes[14]. In the case of SWCNTs, they are just one wrapped sheet of graphene while MWCNTs could be considered as a group of concentric SWCNTs, and whose properties, diameter and length are very different[15]. The dimensions of MWCNTs typically are around 2-20 nm and 1-3 nm of outer and inner diameter respectively with an intertubular distance slightly larger than the graphite (0.34 nm)[36]. In order to describe SWCNTs. SWCNTs is formed when a rectangular area of graphene is rolled (see Fig. 2.3).
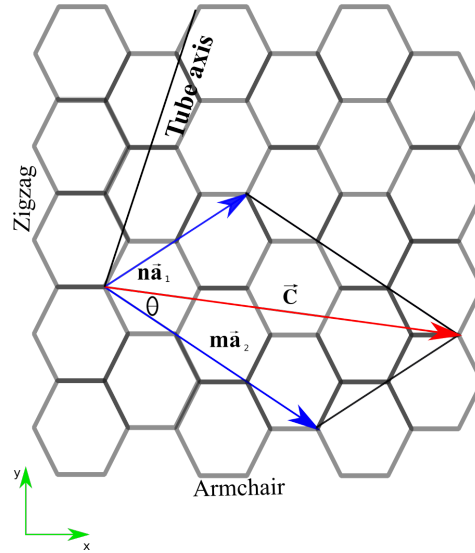
Figure 2.3: Honeycomb lattice of graphene with the unit vectors a_1 and a_2, chiral angle (θ), and the traslational ($\vec{T}$) and chiral vector($\vec{C_h}$). The armchair and zigzag CNTs depends on the (n,m) configuration (based on Anwar, 2011).

The unit cell of SWCNTs is described by the traslational vector $\vec{T}$ and the chiral vector $\vec{C_h}$ which forms an angle called the chiral angle θ. $\vec{T}$ is obtained by the linear combination of the lattice vectors $\vec{a_1}$ and $\vec{a_2}$, and $\vec{C_h}$ is perpendicular to the nanotube axis[2] as it is showed in Fig.2.3. CNTs are only described in terms of the integers (n, m) which corresponds to the number of unit vectors in the crystal lattice[45]. They are called zig-zag if $m = 0$, and armchair if $m = n$. The n, m give information about the metallically and semiconductor character of CNTs, if $n = m$ CNTs is metallic and if $n - m$ is a multiple of 3 CNTs are semiconducting[45]. Carbon atoms in CNTs and graphene have a sp^2 bounding coordination and it is possible to compare many physical and electronic properties between them[2]. However, when a 2D graphene sheet is wrapped into a 1D carbon nanotube, the zero band gap energy can change, it introduces additional quantizations of the band structure of graphene[2].

2.2.1   Properties and applications of carbon nanotubes

Carbon nanotubes have the versatility to be either metallic or semiconductors depending on its structure as it was mentioned before, the corresponding band gap between the conduction band and the valence band is 0 eV for metallic SWCNTs and in semiconductor CNTs the value is between 0.4 and 0.7 eV in semiconducting SWCNTs while in MWCNTs the semiconducting tubes act as semi-metallic as a result of the reduced band gap[46]. CNTs have low mass density, large surface area, high tensile strength, high heat conductivity, and high aspect ratio, and they are mechanically stronger than steel and excellent conductors of electricity[46].

Optical properties

When the graphene sheet is rolled to originate the structure of a CNTs, the π orbital becomes more delocalized outside of the CNTs which derive in a σ orbital slightly out of plane[1]. In that case, it must be taken into account the additional quantization arising from electron confinement around the CNTs circumference[47]. It is needed to satisfy the periodic boundary condition of $\boldsymbol{C} \cdot \boldsymbol{\kappa} = \boldsymbol{2\pi q}$ where $\boldsymbol{q}$ is an integer[47]. The electronic band structure of CNTs it is obtained along the allowed $\boldsymbol{\kappa}$ lines by the superposition of the cuts of the graphene electronic energy bands[47]. The CNTs will be metallic when one of these cuts contains the K point, otherwise CNTs will become semiconductors[47]. In that manner, for metallic CNTs $n - m = 3k$ and for semiconductors $n - m \neq 3k$ where k is an integer. In Fig. 2.4 it is showed the band structure and the Density of States (DOS) of a metallic and a semiconducting CNTs[47]. The sharped peaks (c_1 and c_2 at the conduction band, and v_1 and v_2 at the valence band) in the DOS corresponding to the cuts that originate from the additional level of quantization and are known as Van Hove singularities[47]. these singularities are characteristic of one-dimensional quantum conduction and are not present in three-dimensional graphite-structure caused by the confinement of electronic and phonon states[1,46].
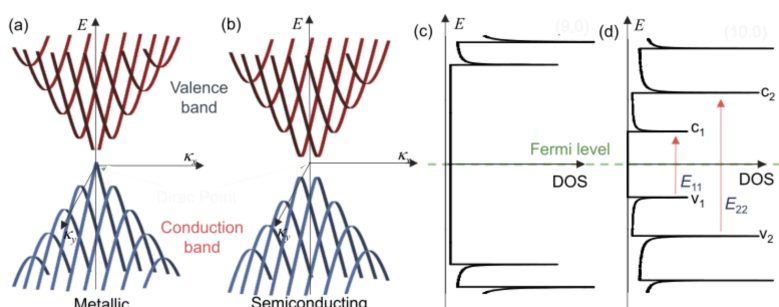
Figure 2.4: Band structure of a) metallic CNTs and b) semiconducting CNTs. DOS of c) metallic CNTs and d) semiconducting CNTs (adapted from Yamashita, 2019).

Electrical properties

The electrical properties of CNTs have a lot of interest in the industry[46]. In comparison with copper, CNTs possess higher electrical conductivity due to their low resistance and the minor quantity of defects in their structure[46]. The range of the electrical resistivity of CNTs is around 10^{-6} Ωm which can be altered by the modification of the CNTs lattice[46]. The introduction of various molecules in the surface of CNTs cause alterations in the electrical conductivity and the Fermi level is sensitive to the dopant introduced in the system[46]. There exist different kinds of environments of doping like interstitial or substitutional doping[46]. In the first case there is not a substitution of the C atom, but also the dopants are adsorbed at the surface. The C atoms and the dopants remain together by a non-covalent bonding[46]. On the other hand, in substitutional doping, there is a replacement of a C atom and they form a sp^2 bonding which could lead in a transfer of negative charge (donor) or negative charge attained from the CNTs (acceptor)[46]. The significant enhancement in the electrical conductivity of CNTs occurs with the chemical doping and intercalation of

different metals[46].

Mechanical properties

CNTs are stiffer than diamond with the highest Young's modulus and tensile strength. The measure of how stiff or flexible material is can be obtained with Young's modulus while tensile stress is a measure of the amount of stress needed to pull a material apart[46]. The bonding between C atoms is one of the strongest bonds in nature and due to that the axial component of the σ bonding between carbon atoms increases significantly when the graphene sheet is rolled up to form the CNTs[46]. The Young's modulus depends on the diameter and not on the chirality, for SWCNTs (with a diameter between $1 - 2$ nm) and MWCNTs has been reported values of 1 TPa and 1.2 TPa respectively while the value for steel is 0.21 TPa. In SWCNTs bundles the Young's modulus decreases to 100 GPa. In the case of MWCNTs, their Young's modulus is higher than SWCNTs as a result of different nanotube diameters contained coaxially and Van der Waals forces acting between the tubes[46]. The tensile strength can be as high as 150 GPa for individual CNTs assuming it has Youngâs modulus of 1 TPa. Additionally, the elastic response to deformation of CNTs is extraordinary because they do not break or fracture when they are severely bent as a consequence of the small number of defects present in their structure. CNTs can be twisted and sustain large strains of 40% in tension before fracturing, in contrast to most of the materials that fail with a strain of 1% or less which is attributed to the propagation of dislocations and defects. The reason for this property in CNTs is the possibility to rehybridization of the sp^2 bond in the hexagonal lattice when the nanotube is bend.

Nanocomposites of carbon nanotubes

The hardness of CNTs has been studied showing that the addition of MWCNTs increases the hardness of a host material. It is attributed that MWCNTs enhances in strengthening and hardening the matrix by increasing the matrix alloy dislocation density during cooling to room temperature[48]. Besides, the difference between CNTs and the matrix in the thermal expansion coefficient is attributed to the increase in hardness. Also, it was reported a decrease in the density of an nanocomposites made with CNTs which is attributed to the porosity increase by the addition of the lightweight and high volume CNTs compared with the matrix[48]. In other research, it was found that the addition of MWCNTs increases the tensile strength in nanocomposites. This was partly attributed to coupled effects of increases in grain boundary area as a result of grain refinement, the strong thermal stress, and the effective transfer of tensile load to the uniform distribution of MWCNTs. However, when the amount of MWCNTs added in the nanocomposites overpasses the optimal value (1.5 wt. %), the nanocomposites become more brittle[48].

Anwar[2] has reported several fascinating applications for CNTs. For example, the electrical, optical, mechanical and electrochemical properties of CNTs could serve to make nanotube-based sensors which are used to do pressure, gas, flow, thermal, optical, mass, position, stress, strain, biological, and chemical measurements[2]. This is based on the fact that CNTs use less power and have high sensitivity to variations in temperature than traditional sensors. Moreover, aligned MWCNTs in silicon chips has shown a higher axial thermal conductivity which allows having a high cooling efficiency which has a great impact as heat dissipator for microprocessors[2]. Besides, thin MWCNTs have been used to fabricate relatively low-cost large area field emission displays. This field emission can be enhanced

with the dopping of MWCNTs with nitrogen, and low thresh hold voltage and higher current densities with a boron doping[2]. Finally, CNTs are the first option for mechanical reinforcement of polymers and composites due to their extreme toughness-to-weight ratio[49]

CNTs have been used to perform nanocomposites with some kinds of clays. Among of these clays are Smectite, Montmorillonite, and Kaolinite. There are some researches that reported nanocomposites made of carbon nanotubes and clays with outstanding properties and applications. Song[27] have used MWCNTs functionalized with polydiallyldimethylammonium chlorideand and hydroxyl-functionalized Montmorillonite to prepare a hybrid nanofiller and integrated it into elastomer nanocomposites using a simple and versatil solution mixing preocess[27]. They also prepared elastomer nanocomposites with styrene-butadiene rubber which improved mechanical, thermal, and electrical properties[27]. They presented the hybrid nanofiller as a novel networked reinforcement which offers the opportunity for preparing high-performance elastomer composites[27]. Another kind of nanocomposites have been reported using amino-functionalized organophilic montmorillonite and carboxyl-modified MWCNTs. Sedaghat[28] showed that the modification of the clay could change its hydrophilicity become it more hydrophobic for the intercalation[28]. Their results showed a uniform disperse and unique morphology of the nanocomposites and they conclude that it is favorable to use nanosponges of these nanocomposites for oil split remediation[28].

Simari *et al.*[29] developed a hybrid materials of CNTs rooted on smectite clays to introduce them into perfluoro-sulfonic acid (Nafion®) membrane and they proposed it as hybrid nanoadditives[29]. They used solution-precipitation method and the structural and morphological studies prove the successful synthesis of the nano-additives and the reaction of highly homogeneous membranes[29]. They showed that the best nanocomposite membrane was made with the oxidation and organo-modification with alkyl-sulfonic groups of CNTs which show a significant effect on the proton transport properties[29]. It reached values of about $2 \times 10^5 cm^{-5} sec^{-1}$ which is three orders of magnitude higher than filler-free Nafion. The proton conductivity that Simari *et al.*[29] reported is $7 \times 10^{-2} S cm^{-1}$ which is very high compared with literature[29]. Finally, they reported that the produced membranes with the hybrid nano additives have higher solidity and extends their thermal stability[29]. They proposed this modified membranes for proton exchange membrane fuel cells[29]. On the other hand, Kaolinite has been used as a substrate to growth CNTs with interesting structures[30].

Mohammadi *et al.*[30] used macroporous kaolin substrates to growth CNTs films via chemical vapor deposition that have heart-like caps. They observed that at higher temperatures overgrown humps grown over the surface of a thin continuous mat-like film of long CNTs. Also, They reported that with an increase of temperature an enlargement the overgrown humps and an increase in their arealCNTs density, a length and average diameter increase of CNTs[30]. Finally, they conclude that the improvement of the vertical alignment of the CNTs on the macroporous kaolin substrate by optimizing other synthesis parameters are being under investigation.

As it was mentioned in this section, CNTs have a lot of outstanding properties, their structure and size make them have some features that are not presented in other materials like van hove singularities. Also, it was described some applications of CNTs with other materials like clays as nanocomposites with better qualities than the pristine. In the following section, it will be described in detail the structure, and applications of a kind of clay minerals: Kaolinite.

2.3   Clay minerals

Clay minerals are important in the production of engineered materials, petroleum discovery, paper, paint, plastic, rubber, cracking catalyst and ceramic industry; the structure and composition of clay minerals are related to their application in the mentioned industries [5,19]. One property that allows classifying clays as a separate group of silicates is the layered structure [18]. Kaolin is a group of dioctahedral 1:1 layer silicates which consist in two-layered material corresponding to one tetrahedral and one octahedral cation sheet linked by bridging oxygen atoms. The tetrahedra are arranged in the sheets in the form of hexagonal nets, which may be deformed [18]. There are oxygen atoms in the surface of the tetrahedral sheet while in the octahedral sheet there are hydroxyl groups [3]. In the top of the octahedral layer the tetrahedral layer match almost perfectly due to the O-O distance of a coordination of octahedron 0.14 nm which is close to the distance between free oxygen in a net (0.13 nm) [18]. Kaolin includes kaolinite, halloysite, dickite and nacrite clay minerals, and the most important of the Kaolin group is kaolinite (Kaol) [19].

2.3.1   Kaolinite

Kaol is chemically inert, white, plate-shaped, soft, fine in particle size, and low in the surface area. [19]. It is an abundant mineral clay in the nature that consists of dioctahedral 1:1 layer silicate with Al^{3+} in the octahedral sites and a hexagonal arrangement of silica tetrahedrons [18,19]. The theoretical composition is 39.8% of alumina, 46.3% of silica, and 13.9% of water [5]. The chemical formula is $Al_2Si_2O_5(OH)_4$ which space group is C1 and the parameters of its unit cell are: $a = 5.154$Å, $b = 8.942$Å, $c = 7.401$Å, $\alpha = 91.69°$, $\beta = 104.61°$, $\gamma = 89.82°$ [4]. The thickness of the silica layer is 0.437 nm and the distance between them is 0.72 nm [50]. In the primitive cell of Kaol, there are four OH groups that are distinguishable. One OH group is located inside the layer and it is almost perpendicular to the next layer is responsible for the hydrogen bond while the other three OH groups are located at the inner surface of the layer. In the case that OH would be parallel to the layer, there will be no hydrogen bonding with basal oxygen atoms of the adjacent Kaol layer [18].
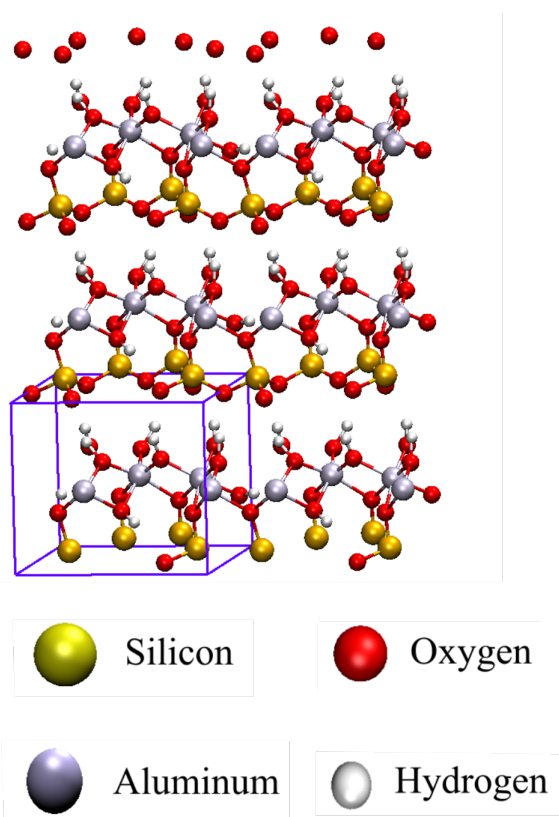
Figure 2.5: Representation of three layers of Kaolinite and its unit cell is showed with the blue box. Aluminum atoms are in grey color, silicon atoms are in yellow-golden color, oxygen are represented with red, and hydrogen are the white spheres

Kaol presents some interesting properties such as absorption, high aspect ratio, and thermal conductivity, high cation exchange capacities, the large surface area which made it a good candidate in the production of materials with novel physical and chemical properties [3,20]. Elimat *et al.* [51] have reported a decrease in the energy gap in a composite made of Kaol and polycarbonate comparing with a pristine polycarbonate pristine matrix. Also, the presence of Kaol in polycarbonate matrix provoked an increase in the thermal conductivity of with a temperature increase due to thermal activation of the phonons. Lattice vibration and electrons make a heat transfer during the thermal activation which induces the thermal enhancement [51]. Similarly, Kaol composites have been studied to waste treatment approach. It was reported a composite made of Kaol and TiO_2 to remove methylene blue (MB) and orange II (OII) by adsorption and photocatalysis. The pristine clays showed MB removal exceeding 90% after just 20 min of contact time while for OII was less than 10%. In the case of Kaol and TiO_2 composite, the removal increased to 95% for MB and 80% for OII [22]. Sempeho *et al.* [52] have taken in advanced the layered structure of Kaol which allows holding water and other organic molecules between the silicate layers to make intercalated nanocomposites

of Kaol with urea and then encapsulating the intercalation compound with gum arabic biopolymer for the purpose of preparing urea control release fertilizers[20,52]. Finally, It has been reported the development of nanocomposites of Kaol and CNTs with adsorption property applications[34]. The preparation of this composite involves chemical modification of Kaol with hexamethylenediamine and HCl, while CNTs was modified with HNO_3.

Microscopic and Spectroscopic techniques are commonly used to characterize composites based in Kaol. The surface morphology, particle shape, and thickness are carried out by Scanning electron microscopy Scanning Electron Microscopy (SEM)[22,52]. Fourier Transform Infrared Microscopy (FTIR) and Raman spectroscopy is used to observe vibration modes of the hydroxyl stretching region, the SiO stretching region, the hydroxyl deformation region[53]. It has been reported other characterization techniques like thermogravimetric analysis (TGA), nuclear magnetic resonance (NMR) or X-ray fluorescence (XRF) spectroscopy which have more specific approaches[22,52].

2.3.2   Composites of Kaolinite and Carbon Nanotubes

Several types of research have been developed using carbon nanotubes and clays. Among the most used clays are Kaolinite, montmorillonite, nontronite, and sepiolite which have been studied extensively and using different methods of synthesis. Kaolinite and montmorillonite were used as a stabilizer of surfactants in MWCNTs solutions[54]. Also, microcrystalline phyllosilicates were synthesized with kaolinite, nontronite, and sepiolite resulting in aligned and not-aligned growth[55]. Besides, clays have been modified to create new bindings, it has been achieved with reactive like dimethyl sulfoxide (DMSO), hexamethylenediamine, HNO_3, H_2O_2, and others[34,54–56]. The main applications of these nanocomposites include treatment of pollution in water and transport in soils and sediments[34,54–56].

Han *et al.*[54] used clay (kaolinite and montmorillonite) in MWCNTs suspensions as a stabilizer of surfactants. They compared the adsorption capacity of three surfactants: cetyltrimethylammonium bromide (CTAB), dodecyl benzene sulfonic acid, sodium salt (SDBS), and octyl-phenol-ethoxylate (TX100) between both clays[54]. Surfactants establish four possible mechanisms which could affect the stabilization of MWCNTs suspensions by: (1) releasing some ions from the minerals into the suspensions, (2) changing the pH value of the suspensions, (3) suppressing the suspensions by their surfactant sorption, and (4) adsorbing the suspended MWCNTs directly. Further research involves the use of CNTs in the preparation of nanocomposites based on kaolinite.

Nanocomposites made of Kaol and MWCNTs with the potential application in water treatment have been reported by Yadav *et al.*[34]. They applied a chemical treatment into Kaol and MWCNTs to obtain -NH$_2$ and COOH bonding respectively, and at the end, they obtained CONH bondings[34]. The process of preparation that they reported is as follow: Kaol was mixed with deionized water, heated, and mixed with hexamethylenediamine and HCl, filtered, washed, and dried[34]. They sonicated MWCNTs in ethanol, filtered, dried, and then, they mixed the MWCNTs with $3.0M$ HNO_3 and 30% v/v H_2O_2 by stirring, and they filtered and washed it again. Yadav *et al.*[34] prepared the mixture of Kaol and MWCNTs by sonication of the treated Kaol with Dimethylformamide (DMF), and then, they added the MWCNTs. Finally, they reported that the solution was heated, refluxed, filtered, washed. and dried[34]. In the results that Yadav *et al.*[34] presented, the -NH$_2$ and COOH bondings were confirmed by FTIR, the structural properties by X-ray Diffraction (XRD), also there was made SEM, High Resolution Transmision Electron Microscopy (HTEM), and Brunauer-Emmett-Teller (BET) surface area for pore size distribution[34]. They used the FTIR to confirm the

CONH functional group on to the surface of nanocomposites and they supported this result with XRD, SEM, and HTEM analysis[34]. They conclude that the nanocomposites have got better adsorption capability for water treatment thus it has potential application for removal of pollutants from waste water[34].

Other applications of carbon nanotubes with kaolinite

Carbon nanotubes/clay nanocomposites have been synthesized via hot filament chemical vapor deposition[55]. Pastorková *et al.*[55] used Kaolinite, nontronite, and sepiolite as carrier minerals, and particles of ion were incorporated as the active phase. They performed the experiment in a reactor employing the double bias-assisted (or dual plasma) hot filament chemical vapor deposition method, above the substrates, they placed five tungsten filaments. They characterized the nanocomposites by Transmission Electron Microscopy (TEM), High-resolution transmission electron microscopy (HRTEM), Energy-Dispersive X-rays Microscopy (EDS) and Selected Area Electron Diffraction (SAED). Pastorková *et al.*[55] reported doping of Kaolinite and sepiolite by a catalytically active metal. The research carried out a successful synthesis of CNTs on three types of microcrystalline phyllosilicates. They observed that when Kaolinite was used, CNTs grow through the whole volume and create 3D grids and in the cases of nontronite and sepiolite, the CNTs grow through the volume of the mineral but also create a clearly identifiable separate phase. The growth in nontronite was not-aligned while in sepiolite it was[55].

Nanocomposites for the removal of Fe and Mn from aqueous solutions and natural underground water have been reported. these nanocomposites were synthesized of metakaolinite/carbon nanotubes (K/CNTs) and kaolinite/starch (K/starch)[56]. The K/CNTs nanocomposites were prepared via Kaol modification with DMSO and stirred to after washing with isopropanol and distilled water and finally, it was dried. The K/starch nanocomposites were performed on one hand dispersing Kaol with DMSO in distilled water and on the other hand, starch was dissolved in distilled water and added to Kaol. Finally, the mixture was filtrated, washed, dried, and ground. It was analyzed the adsorption as a function of pH, contact time, initial concentrations, adsorbent masses, temperature. Moreover, it was made several kinetic and isotherm models to investigate the adsorption mechanisms[56]. XRD, SEM, and TEM techniques were used to characterize the mentioned nanocomposites and it was found that neutral pH from 6 to 7 is the optimum pH for the removal of the Fe and Mn metal ions by K/CNTs and K/starch. The thermodynamic studies suggest that K/CNTs nanocomposites reflected for the adsorption an endothermic nature while K/starch reflected an exothermic nature. It was tested in water contaminated by $0.4 mg/L$ iron and $0.5 mg/L$ removing 92.5% and 72.5% from the iron using 20 mg of K/CNTs and K/starch nanocomposites, respectively. K/CNTs was more efficient than K/starch in the removal of Mn ions. Depending on the surfactant, it is possible to be selective in their transport in soils and sediments[56].

An interesting modification of MWCNTs was made by Kumari *et al.*[57] by irradiated MWCNTs with high-energy Au^{+8} ions (100 MeV) reporting sp^2 to sp^3 hybridized carbon transformation. They characterized the medicated MWCNTs with Raman spectroscopy, X-ray Photoelectron Spectroscopy (XRP), and HTEM. The main feature that suggests the transformation in the hybridization is the apparition of a new peak in the Raman spectrum at $1543 cm^{-1}$ associated with the *G* peak in tetrahedral amorphous carbon (t_{a-C}) and the vanishing of $2D$ band[57]. Also, they observed broadening in D and G, with a slight shift in their positions and consistent decrease in 2D band intensity, as fluence increased.

2.4 Characterization and sample preparation techniques

2.4.1 Raman spectroscopy

The basic principle of the Raman process is when monochromatic light is elastically scattered by matter[33,58]. Visible light could be considered as a propagating oscillating dipole which is larger than the one of a molecule as a result of the difference in the size of the molecule and the wavelength of light[59]. When light passes through a molecule, the electrons become polarized achieving a higher energy state in which energy of the light wave is transferred to the molecule creating a virtual state or also called a very short-lived "complex" that is not stable[59,60]. It does not involve a nuclear movement and the way to achieve the most stable energetic level, energy is released in the form of scattered radiation[59]. This kind of scattered radiation does not show an appreciable change in energy and it is called Rayleigh scattering in which a photon interacts with a molecule elastically (see Fig. 2.6 a)[59]. Raman scattering involves the movement of the nuclei which are heavier than just the electronic cloud and shows appreciable changes in energy[59]. It could occur by either giving energy up or by removing energy from the molecule[58]. The light that suffers an inelastic lost of energy is denominated Stokes scattering and the light that has a gain of energy is called anti-Stokes scattering[58,61]. It is showed in Fig. 2.6, the blue arrows represent the incident radiation and the red, violet, and green arrows represent the scattered radiations. b) represents the Stokes Raman scattering in which the scattered radiation is less than the incident radiation and c) represents the Anti-Stokes Raman scattering in which the energy of the scattered radiation is more than the incident radiation. Raman scattering is an event which involves only one in $10^6 - 10^8$ of the photons scattered, and Stokes bands are used in Raman spectroscopy as they are more intense than the anti-Stokes bands involving transitions from lower to higher energy vibrational levels[59,62]. the Raman effect measures to wave-numbers derived from light scattering that gives information about the energy levels of the molecule due to it is caused by a change in the rotational and vibrational energy of the molecule[33,61].
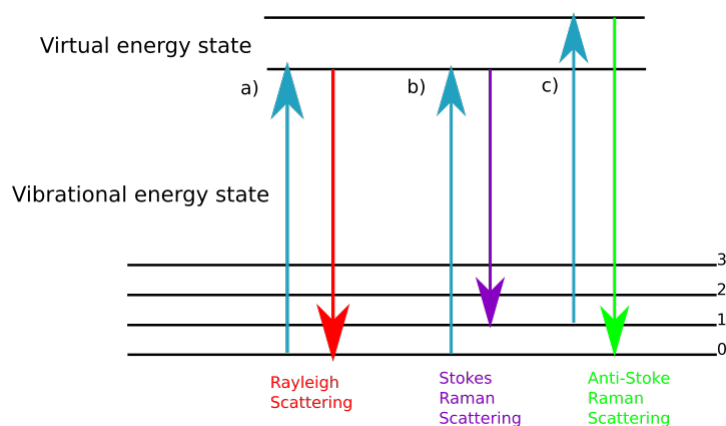

Figure 2.6: Diagram of energy-level showing the states involved in Raman spectra where Rayleigh scattering does not lose energy, but Stoke and anti-Stokes Raman scattering are produced with a loss of energy (based on Potcoava *et al.*, 2014).

The basic function of a Raman system uses an excitation source of light in the visible range to the sampling point, disperse and detect the scattered light, and represent the spectral data graphically or mathematically[64]. To accomplish these requirements, the major components in a Raman system are lasers, sample illumination system and light collection optics, wavelength selector which could be a filter or a spectrometer, and a detector[65]. The system that absorbs or emits energy make it in a quantized form called phonons (interpreted as vibrations)[41]. Fig. 2.7 shows an scheme of the Raman spectrometer with the basic components.
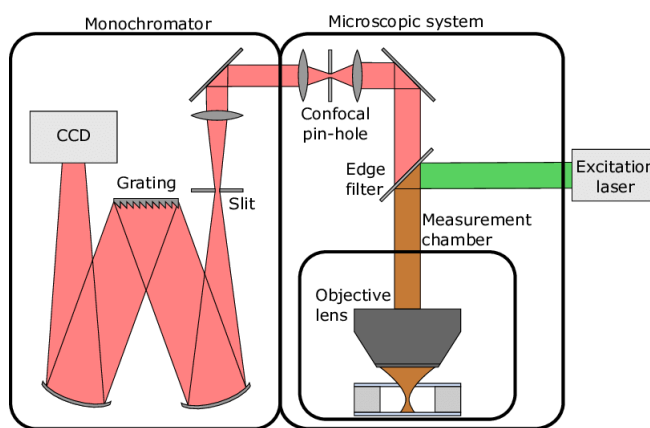

Figure 2.7: Raman spectrometer scheme (source: Karlen, 2018)

Normally, the sample is illuminated by a laser beam due to their highly monochromatic nature and high beam fluxes which are in the near infrared, visible (Vis), or ultraviolet (UV) range[60]. Despite the Raman measurements are independent of the wavelength of the laser excitation, it is important to consider some aspects like fluorescence, band intensity, spectral resolution and range, and spatial resolution. Fluorescence could mask the Raman spectrum, but it can be avoided using the correct wavelength[60,67]. The band intensity is higher when the wavelength of the laser is smaller since the amount of scattered light is strongly dependent on the wavelength ($I_{Rayleigh} \propto \lambda^{-4}$)[67]. Besides, it is not possible to obtain the widest range and the better resolution at the same time. As a result of the inverse proportionality between energy and wavelength, a short laser wavelength in just one measurement can cover large spectral range decreasing the spectral resolution and viceversa[68]. Finally, by reason of the diffraction limit, the spatial resolution depends on the laser wavelength approximately by:

$$S\,potsize \approx \frac{1.22 * \lambda}{NA} \tag{2.1}$$

where NA is the numerical aperture if the lens and λ is the wavelength of the laser[68,69].

The Raman scattering is very weak compared with Rayleigh scattering, and in order to separate these signals, filters are used[70]. Three basic types of filters there are for Raman spectroscopy systems. Laser-line filters are used as laser transmitting filters which block any undesirable light from the laser and it is located between the laser

and the sample block[71]. Then, in order to block the Rayleigh scattering edge filters or notch filters can be used[72]. Notch filters block the specific range in which the Rayleigh occurs while edge filters block either all the spectra until Rayleigh light or all the spectra since Rayleigh light[71].

In the spectrometer, the stray light is generated mainly upon light dispersion in gratings and strongly depends on gratings quality[73]. The spectrometer separates the different radiation and consists of an array of finely spaced lines or grooves on a reflective surface[70,74]. Destructive and constructive interference occurs due to this process is wavelength and angle dependent, thus each wavelength is reflected at a different angle[74]. A pin hole is used to ensure a confocal image[68]. A spectrum with higher resolution can be achieved with a grating with a higher number of groves per mm, but it covers a less spectral range[75]. The gratings are optimized over a relatively narrow wavelength and it must be selected for the desired resolution and for each laser[68].

Finally, the signal achieve the detector which converts it to a digital signal[70]. The earlier detector used was a photomultiplier tube, then image intensifier vidicon camera, intensified photodiode array, and currently charge-coupled device (CCD)[65,76]. In CCD detectors each element (pixel) of the detector is a photoactive capacitor which based in the number of photons that strike it collect and hold charge[70]. Each pixel at a given wavelength and a variable quantity of photons is a specific resolution element[75]. In that manner, it is possible to associate noise to each detector element, a reduction of the noise can be achieved decreasing the temperature of the detector[70].

Raman spectroscopy has become a powerful and nondestructive technique to characterize carbon materials[44,49,77]. It is widely used to characterize pyrolytic graphite, carbon fibers, glassy carbon, pitch-based graphitic foams, nanographite, ribbons, fullerenes, carbon nanotubes, and graphene[44]. It provides information about crystalline size, clustering of the sp^2 phase within a given sample, the presence of sp^3 hybridization and chemical impurities, its mass density, optical energy gap, elastic constants, doping, defects and other crystal disorder, edge structure, strain, the number of graphene layers, nanotube diameter, nanotube chirality and nanotube metallicity behavior[49].

Raman characterization of carbon nanotubes

One of the most powerful tools to characterize CNTs is Raman spectroscopy[15]. The reduced dimension of CNTs causes that its Raman spectrum is unique and significantly different from the spectrum of other carbon allotropes[1]. Via Raman spectroscopy many fundamental aspects of CNTs have been studied like the optical response, the presence of $sp^2 - sp^3$ hybridization, elastic constant, defects, edge structure, nanotube diameter, chirality, curvature, metallicity behavior, crystal size, electronic and vibrational properties[2,44]. Raman spectroscopy could help to proof modifications on the CNTs surface that includes the introduction of surface species as well as the charge-transfer effects caused by doping[78]. The mass of the atoms, and the strength of the bonds influence the vibrational frequencies in CNTs[78]. The main features that appears in Raman spectrum of CNTs are the Radial Breathing Mode (RBM), the D line, the $G-$line (it could be split into G^+ and G^-), the G'line, and a combinational mode of D and $G-$ line that appears between 150-550 cm^{-1}, 1240-1450 cm^{-1}, 1500-1600 cm^{-1}, 2450-2650 cm^{-1}, and 2775-2950 cm^{-1} respectively[15,41]. A characteristic Raman spectrum of MWCNTs is shown in Fig. 2.8 which was adapted from the research by Zdrojek *et al.*[79]. Fig. 2.8 shows the characteristic peaks of MWCNTs in the frequencies that were mentioned before. In order to understand the origin of these characteristic features in CNTs, it is needed to go deep in the scattering process.
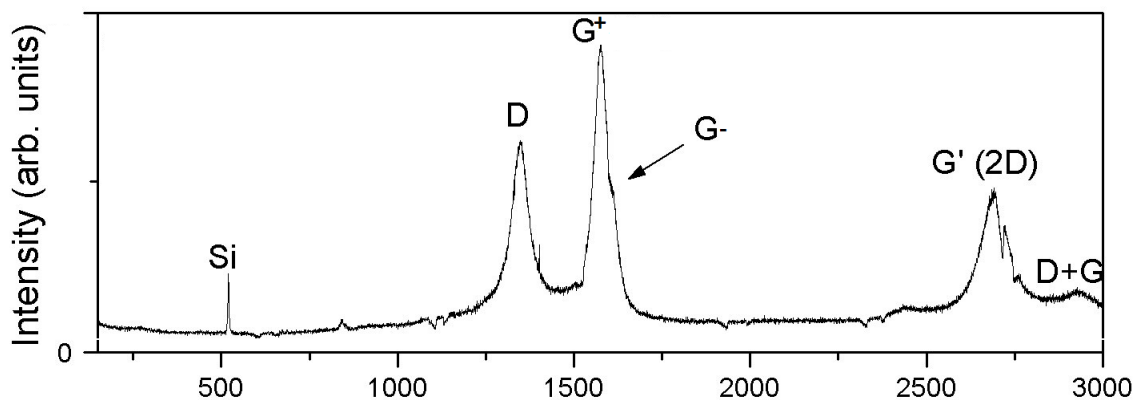
Figure 2.8: Characteristic bands of a Raman spectra of MWCNTs in which appears the D, G^+, G^- G' or $2D$, and $G + D$ lines (adapted from Zdrojek *et al.*, 2004).

A resonance Raman effect occurs when the laser energy matches the excited states of the CNTs causing that the Raman spectrum becomes sharper, the non-resonance Raman scattering is not observed because it is too weak [1,49,80]. The explanation is that in CNTs there is a large number of electrons in each nearly discrete level (a Hove singularity) which can absorb light at the resonance frequency [1]. The order of the Raman process depends on the number of phonons that are emitted, first and second order Raman process are the most used to explain the characteristic feature of CNTs and in general allotropes of C [41,81].

First and second-order Raman process is shown in Fig. 2.9 a). The first Raman process occurs when a photon excites an electron from a state i to a real electronic state m, the light absorption is the resonance process. After that, a phonon with $q \approx 0$ and frequency ω_q scatter the photo-excited electron to a virtual state m' and decay to the initial i state [81]. In the second order Raman process (Fig. 2.9 b) a photon excites an electron (with wave vector **k**) from the valence band to the conduction band vertically in momentum space. It is scattered to a m' state emitting a photon (with a wave vector **q**) in the process, it is located at $k - q$ state [81]. A second photon (with wave vector **-q**) is emitted and an electron goes back to another virtual state m'', and finally, the electron comes back to the initial state emitting a photon allowing a momentum and energy conservation [81]. If the scattering phonon process occurs in the same valley it is called intravalley scattering while the process that involves two valleys **K** and **K'** points in the Brillouin zone corresponds to an intervalley process [81]
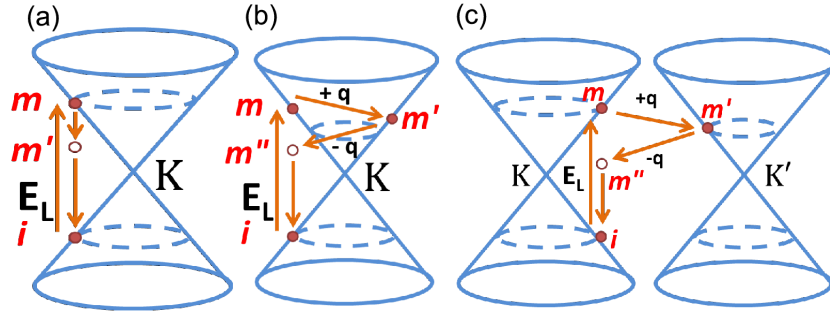
Figure 2.9: a) First Raman process where the electron is exited from the state i to the real electronic state m, a phonon scatters the photo-exited electron to the virtual state m' and decay to the state i b) intravalley second Raman process occurs in the same valley where a photon excites an electron to the state m and scattered to the state m' emitting a photon, a second photon is emitted when the electron goes to another virtual state m'', and finally, the electron comes back to the initial state emitting a photon c) intervalley involves two valleys (**K** and **K'** points in the Brillouin zone), but the process is the same as the intravalley second Raman process (source: Siregar, 2015).

The RBM is a first-order Raman process that is a characteristic features of SWCNTs and can give information about the diameter [15,41,44]. All the carbon atoms move coherently in the radial direction in plane perpendicular to the nanotube axis corresponding to a bond-stretching out-of-plane phonon mode [41]. The diameter of the SWCNTs is inversely proportional to the frequency of the RMB by: $\omega_{RMB} = C/d_t (cm^{-1})$ with $C = 248cm^{-1}nm$ for isolated SWCNTss on a SiO_2 substrate. Since the mass of all the carbon atoms along the circumferential direction is proportional to the diameter, this relation is possible [41].

The D and $G'-$ bands have a similar mechanism that activates them in the Raman spectrum: a double resonance mechanism [1]. The formation of the D band occurs by the coupling of electrons and phonons which carries information about the crystallinity quality id the samples. It appears for sp^2 carbons and in the presence of vacancies, grain boundaries, hetero-atoms, or any defects that reduce the crystal symetry [1,2]. The difference between D and G' is that D band involves a phonon and a defect while G' involves two phonons at wave vector **q** and **-q**. D band corresponds to a first-order scattering process which passes information about the defects present in the lattice. An increase in the intensity of the $D-band$ can be interpreted as an increase in defects. These defects could be the formation of pentagons-heptagons pairs (topological), rehybridization between sp^2 and sp^3, vacancies,in-plane substitutional hetero-atoms, dislocations, a doping [2]. It is possible to see shifts in this band as it is laser energy dependent [45] and it is a predominant band in the Raman spectrum of CNTs [43]. An overtone of D band appears in the range of $2775 - 2950cm^{-1}$ that corresponds to a second-order Raman scattering called G' or $2D$ line, but this band could appear even if the D line does not [43]. The $G-$ band that appears around 1580 cm^{-1} is a first-order Raman peak which could split into G^+ and G^-, in contrast to graphene that has only one in-plane vibrational mode.

The initial electrons have a wave vector and a scattered electronic state whom wave vectors are κ (measured from the K point in the reciprocal lattice of graphene) and $\kappa + q$ respectively with **q** as the phonon wave vector [1]. It mus satisfies the energy-momentum conservation relation that is showed in Eq. 2.2 where the Stokes and anti-Stokes

process corresponds to the $\pm$ factor.

$$E(\kappa + q) = E(\kappa \pm \hbar\omega_{ph})(q) \tag{2.2}$$

The later also requires to lead a relation between the κ and for electrons and q for phonons. Two possible equi-energies $E(\kappa + q)$ are required for energy and momentum conservation, where the electrons have $\kappa + q$ wave vectors[1]. One exists around the K point as the initial state κ and the second is located around K' point which corresponds to an intravalley and an intervalley process respectively. Once the incident photon is absorbed and scattered by phonons, impurities and defects scatter elastically electrons from the state $\kappa + q$ go to a final state with a wave vector κ, the electron-hole pair is created and the phonon is scattered[1]. In the case of the G' band in which two phonos are involved with q and $-q$ wave vector, arrive to the final state inelastically scattered from the $\kappa + q$ state with a wave vector κ[1]. A double resonance process that satisfies Eq. 2.2 is found near to $|q - q_0| \sim 2\,\kappa$ which are preferentially located the q values that strongly contribute to the double resonance process where q_0 is the phonon wave vector between K and K' points in the 2D FBZ. G' band strongly depends on compressive and tensile strain[1]. Another band that could appear due to defects is the called $D + G$ band which appears around 2900 cm^{-1}.

The more intense peaks correspond to G^+ and G^- and result from in pane vibration of C atoms in the lattice[15]. Unlike graphene, in CNTs the two possible transverse mode phonons are different between them due to the axis of the CNTs is the reference of vibration motions[15]. In that manner, the phonons in the direction of the tube axis correspond to the G^+ while the transversal phonons generate the G^- band. G^+ band is independent of the diameter or chiral angle while G^- is dependent on the diameter but not of chiral angle[41]. In the data treatment, when the CNTs are semiconductors G^- can be fit with a Lorentzian line shape while for metallic CNTs a Breit-Wigner-Fano (BWF) line shape is used[15,41].

After understanding these processes and their origin, it is expected that any attachment of chemical species provokes a perturbation in the Fermi level of CNTs through charge transfer effects[1]. As a result of the strong coupling between electrons and phonons in the resonance Raman process, it makes sense that such perturbations should be visible in the Raman spectrum bands. In Raman measurements of SWCNTs, it was found that there is an up-shift in the frequency of $RMBs$ and G^+ bands when they are doped with halogen acceptors by ~ 74 cm^{-1} and ~ 24 cm^{-1} respectively[1]. In contrast, there is an up-shift when the doping is made with alkali metals in the RBM and $G-$ line. Shifts in the G^+ lines provides information about charge transfer. The doping with halogens results in an electron transfer from the π state to the halogens creating hole carriers in SWCNTs making them SWCNTs p-type. In the case of alkali doping, they transfer electrons to the π^* state resulting in SWCNTs n-type doped. Theoretically, explanations involve a rigid band model, and it suggests that the Fermi level is shifted with the addition of electrons or holes[1]. Another important feature is that the quality of crystal structure in CNTs can have a quantitative value using the ratio of integrated intensities from the D to $G-$ band (I_D/I_G). Lower the (I_D/I_G) ratio, higher will be the quality of graphite lattice[2]. Bokobza and Zhang[77] reported the behavior of the Raman bands of MWCNTs when they undergo dispersion methods such as sonication in cyclohexane. They found that the bands suffer an up-shift due to disentanglement and subsequent dispersion[77]. A piece of additional information about crystallinity could be obtained with the Full Width at Half Maximun (FWHM) of the $G-$ band. It was reported that the decrease of the FWHM of the $G-$ band is an indicator of the crystallinity of the CNT[82].

A complementary tool of Raman spectroscopy is the SEM which could provide more information about morphology, topography, or defects. Detailed information on the working principle of SEM is presented in the following section.

2.4.2   Scanning Electron Microscopy

This section must start with the definition of resolution which is the minimum distance in which two structures can be separated and still appear as two distinct objects[83]. Mathematically, if D is the distance of resolution, λ the wavelength of imaging radiation, n the index of refraction of medium between the point source to the "detector", and α the half angle of a cone of image formation. then, resolution can be described by:

$$d = \frac{0.612\lambda}{n \sin \alpha} \tag{2.3}$$

The resolution of the human eye in the best case is around $3 - 4mm$. In the "nano" world, this resolution is not enough to study nanostructures. In that manner, regarding Eq. 2.3, the resolution could be enhanced if the wavelength is decreased. However, the human eye is not capable to detect lower wavelengths than the ones in the visible range, techniques were developed to have a better resolution and transformed that into visible signals for the human eye. A source of smaller wavelength are electrons which are in the range of atomic distances, they could interact with matter and being transformed into a visible image which is the physical process behind SEM.

SEM is a technique that allows having topography and topological information of a sample. The basic working principle is that the images are formed scanning the surface of the sample with a beam of electrons which interacts with the matter, loss some energy and carry out information to a detector which produces images by contrast[83]. A conventional SEM is shown in Fig.2.10 and it is formed by an electron optical system to produce the electron source, a specimen stage where the sample is placed, a secondary-electron detector which collects secondary electrons, and an image display unit. An electron gun is placed at the top of the equipment which produces electrons that can be accelerated in a range of energy between 0.1-30 keV[84]. In order to reduce the spot size and to focus the electron beam, electromagnetic lenses and apertures are used. It is needed a high vacuum environment to allow the traveling of the electrons without scattering from the air. Real-time observation and image recording of the specimen surface is possible due to the specimen stage, electron beam scanning coils, signal detection, and processing systems[85].

The formation of images depends on the acquisition of signals generated from the interaction between the specimen and the electron beam. Similar than in Raman spectroscopy, the interaction could be inelastic or elastic with and without loss of energy respectively[83,85]. The incident electron could be deflected by the specimen atomic nucleus or by outer shell electrons of similar energy resulting in elastically scattered. This process involves negligible energy loss during the collision and a wide-angle directional change of the scattered electron. The incident electrons that are scattered with an angle larger than 90° and elastically are called Back-Scattered Electrons (BSEs) and yield useful signals for imaging samples. BSEs posses high energy and can extract information from the deep region of the specimen[83,85]. They are sensitive to the atomic number producing bright images for heavy atoms and darkness images for lighter atoms. However, it can not give information about what element is present, just a qualitative

comparison of the constituent atoms in the specimen. The incident electrons that are scattered inelastically ionize the sample, it means the emission of the valence electrons produces Secondary Electrons (SEs) [83,85]. They have very small energy which implies that the electrons generated at a deep region are quickly absorbed by the specimen and are emitted out of the specimen being generated at the surface. In that manner, SEs are very sensitive to the surface and they are used to image or analyze the topography of the sample. Since SEs have small energy, the potential near the specimen influences it resulting in an anomalous contrast when the specimen is electrically charged. Of course, it generates other signals when the electron beam strikes the sample including x-rays, Auger electrons, and cathodoluminescence for different approaches [83,85].
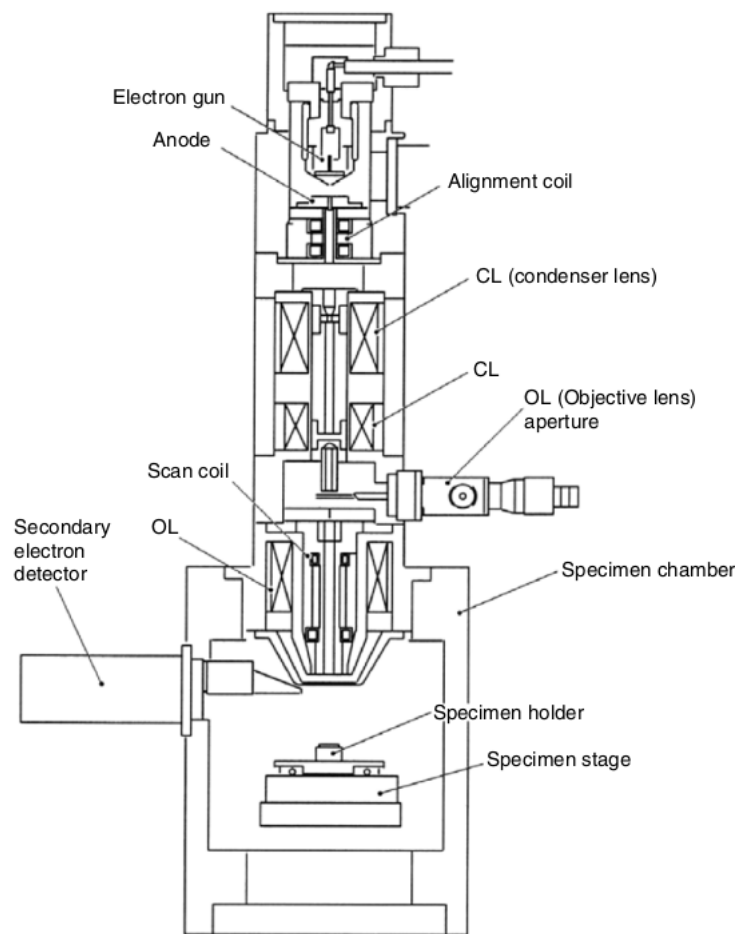

Figure 2.10: Schematic diagram of a SEM (source: Aharinejad and Lametschwandtner, 1992).

The electron gun provides a source of electrons. This is produced when a voltage is applied into a filament which

could be made of Tungsten or Lanthanum hexaboride. The energy of the generated electrons could be tuned in the rage of 1-30 k eV and it passes through a plate with a hole (a system of anode and cathode is formed to allow the pass of electrons)[83]. In order to focus and reduce the spot size of the electron beam produced, electromagnetic or condenser lens and aperture are used. It is applied a magnetic field to adjust the trajectory of the electron beam and it is modulated by the current that passes through the coils that form condenser lens[83,85]. The electron beam diverges after passes through the anode plate, and the condenser lens is used to converge the electron beam and collimated into a relatively parallel stream. Also, the position of the focal point is controlled by adjusting the condenser lens current and the magnification and demagnification are attributed to these lenses. The objective lenses focus the beam into a probe point at the specimen surface and provide additional magnification. In the specimen stage, the sample is placed and it is possible to move in the three directions (x, y, and z)[85]. Once the electron beam interacts with the specimen and the BSEs and SEs are generated, they must be detected and processed into an image. The SE detector is a scintillator (fluorescent substance) and a high voltage about 10 kV is applied in the coated tip to attract the SEs. Then, light is generated which goes to a photo-multiplier tube and converted to electrons which are amplified as an electrical signal. The collector (a supplementary electrode) is placed before the scintillator to help it to acquire SE[83,85]. SEM is used to analyze nanocomposites instead of the light microscope because it allows a higher resolution. The resolution of a light microscope is about 200 nm whereas the resolution of a typical SEM is better than 10 nm, and the topographical detail is better in a SEM than in a light microscope[86]. SEM is a useful technique to obtain morphology, particle size and topography of nanocomposites and it cannot be done with the conventional microscope.

Sometimes it is desirable to analyze CNTs dispersed in any solution instead of in powder. One way to disperse CNTs is the bath sonication, and it will be presented in the following section.

2.4.3   Sonication

The sonication process involves the use of sound energy to move or agitate particles in a sample. Generally, the energy sound used is in the range of ultrasound that corresponds to frequencies higher than 20 KHz[87]. In an elastic medium such as air and the majority of liquids, when the sound waves are transmitted there is a continuous transition while in a non-elastic medium such as water and many liquids the continuous transition occurs when the amplitude of the sound wave is low[87]. However, when the amplitude is increased the magnitude of the negative pressure in the areas of rarefaction (reduction of density) becomes so high and it is possible to cause the liquid to fracture due to it is caused a phenomenon called cavitation (see Fig. 2.11). In the cavitation phenomenon, "bubbles" are formed at sites of rarefaction due to the negative pressure. During the pass of the wave, the "bubbles" of cavitation growing to an unstable size because they oscillate under the influence of positive pressure[87]. Finally, an implosion results from the violent collapse of the cavitation "bobbles" making that the shock waves radiate from the collapsing site[87]. Ultrasound treatment is a feasible technique for treating nanomaterials[88]. In the case of Kaol it is used to facilitate the dehydroxylation[89]. It causes sonication a significant particle size reduction by delamination and lateral breaking of the layers[89]. On the other hand, the dispersion of CNTs can also be promoted with sonication as well as the enhancement of their solubility[90] as it will be explained in the Chapter 4

Compresion waves

−sound pressure +

compression   compression   compression   compression

amplitude

expansion   expansion   expansion   expansion   expansion
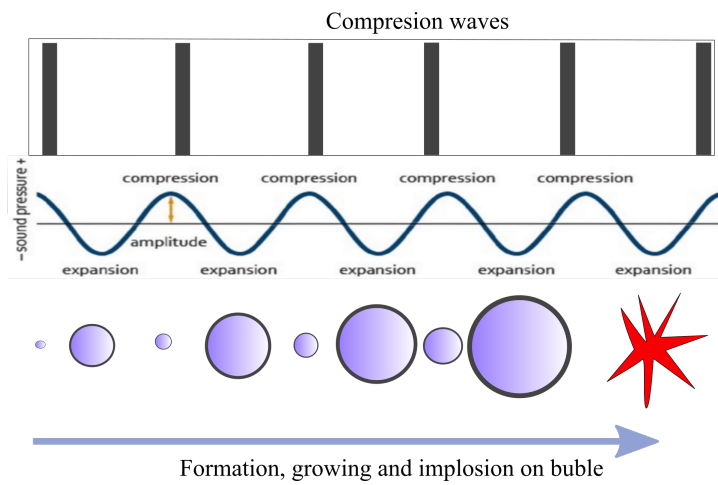
Formation, growing and implosion on buble

Figure 2.11: Cavitation process where the bubbles are formed in the negative pressure of sound, then, they growth until an unstable size and an implosion occurs (based on Johansson *et al.*, 2017).

Chapter 3

Motivation

There exist a lot of research that describes the properties, structure, and modifications of Carbon Nanotubes (CNTs). Undoubtedly CNTs are one of the most amazing nanomaterials with outstanding properties. It has been mentioned in the previous chapter some of the properties that make CNTs a desirable material to produce nanocomposites based on them. Depending on the chirality of Multiwalled Carbon Nanotubes (MWCNTs). The tensile stress and Young's modulus is very high overtaking the values of steel. In the majority of the research were CNTs are used with other materials, the final resulting material received an enhancement in their properties due to the presence of CNTs. Among the applications of CNTs implies the use of them as a reinforcement material. Some research used CNTs with clays to produce nanofillers. Scientist used clays in their research to explore their properties such as their high aspect ratio, high thermal conductivity, large surface area, and others and Kaolinite clay (Kaol) is one of the most clay used in research.

The research that has been reported using Kaol and CNTs has focused on using Kaol as a catalyst or substrate to grow CNTs with some specific feature, such as aligning them horizontally. Only one work has been found in which CNTs are used as reinforcement material in Kaol in which they chemically modify the structure of both Kaol and CNTs inducing bonds with the functional groups that were attached. There are no works that use simple techniques to functionalize Kaol with CNTs such as sonication. Raman spectroscopy allows identifying interactions between the materials of the nanocomposites. However, no studies have been found that analyze in detail the Raman spectra in this type of nanocomposites such as doping, charge transfer, crystallinity or hybridization.

In this work, we prepared nanocomposites using MWCNTs as reinforcement material in a kaolinite clay matrix without chemically modifications to enhance the properties of the clay. These nanocomposites were characterized by Raman spectroscopy and Scanning Electron Microscopy (SEM) microscopy to obtain detailed information on the electronic and vibrational properties of the nanocomposites. It includes charge transfer, doping, crystallinity, hybridization of the carbon atoms morphology, and grain size of the nanocomposites.

Chapter 4

Preparation of Kaol-CNT Nanocomposites and Technical Aspects

This chapter contains the detail information of the preparation of the nanocomposites of Kaolinite clay (Kaol) and Multiwalled Carbon Nanotubes (MWCNTs) as well as the sample preparation for Raman and Scanning Electron Microscopy (SEM) characterization.

4.1   Preparation of the Nanocomposite

The Kaol pristine material was obtained from Cuenca, Ecuador. The reference parameters of this clay were shown in the Table 4.1 which corresponds to chemical analysis of a commercial Kaol obtained from the provider and used as reference analysis. The received Kaolinite was not totally pure with many big particles in the range of cm and with moisture. these conditions are not optimum for the preparation of the nanocomposites. In that manner, the Kaol received material was dried from 24 hours in an oven at 120°C. After that, it was used a ceramic morter to reduce the grains until everything was uniformly dust which takes around $10-12$ minutes. On the other hand, Carbon Nanotubes (CNTs) used were MWCNTs provided from Friedrich-Alexander-Universität Zentralinstitut für neue Materialien und Prozesstechnik (ZMP) with the code of reference is 3100. All the sample were prepared with $1g$ of the pulverized Kaol and the amount of MWCNTs added to each nanocomposite was measured in weight % with respect to the $1g$ of Kaol. In that manner, four nanocomposites were prepared at different concentrations of MWCNTs: Kaol-MW-5%, Kaol-MW-1%, Kaol-MW-0.1%, and Kaol-MW-0.05% which correspond to 5, 1, 0.1, and 0.05 wt.% of MWCNTs. The first step was to disperse Kaol in 10 ml of distilled water in an ultrasonic bath of 100W/42 kHz at room temperature for 10 minutes. Then, the corresponding amount of MWCNTs was dispersed in 10 ml of isopropanol (MWCNTs are not miscible in water) in the same conditions of the ultrasound bath of dispersed Kaol. It was selected isopropanol base in the results of Jagadish *et al.* [92] whom dispersion in isopropanol was good and it is less dangerous than better organic solvents like hexane. Finally, the solution of Kaol was added to the

solution of MWCNTs to avoid the loss of MWCNTs in the container. It is important to disperse first Kaol instead of MWCNTs to prevent possible precipitation of MWCNTs. The final nanocomposites look as in the Fig. 4.1 samples were stored for at least 24 hours before any measurement. The final nanocomposites was sedimented at the bottom obtaining a mixture of water and isopropanol at the top of the vial.
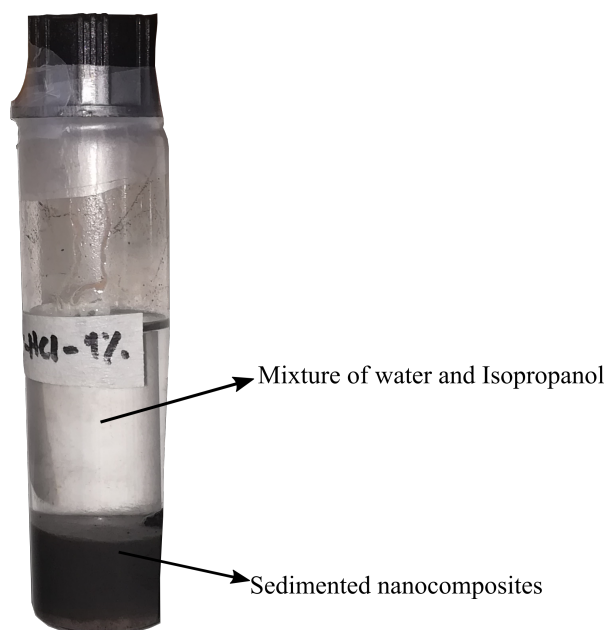
Figure 4.1: Physical appearance of the nanocomposites of Kaolinite and MWCNTs. At the top is a mixture of water and isopropanol, and in the bottom the nanocomposites are sedimented

Table 4.1: Chemical analysis by gravimetry and complexometrics of a commercial kaolinite obtained from the provider

Compound	Percentage content
SiO_2	58-63%
MgO	1.5% max
Al_2O_3	17-19.5%
CaO	3.0% max
Fe_2O_3	2.5% max
TiO_2	0.18 %

4.2 Raman and Scanning Electron Microscopy measurements

Two Raman equipment were used for the measurements: *LabRam Aramis* (R. Aramis) and *LabRam HR Evolution* (R. HR Evolution) with *LabSpect* software. Each sample was taken from the solid part at the bottom of the solution and put in a glass slide microscope (one drop), it was dried in a vacuum oven at 80°C for 12 hours. The detailed parameters of measurement in the Raman equipment are summarized in Table 4.2. The Raman measurements of Kaolinite pristine presented fluorescence which hide all the signals. This issue also has been reported by Michaelian[93] that solved it with a baseline correction and reducing the range of measurement. It also was reported that in powdered samples of Kaolinite it is more difficult to obtain good Raman signals[53]. In that manner, a base line correction with the software measurement was applied in all the Raman experiments, except for MWCNTs sample pristine. The Raman grid used have a measurement range of 600 cm^{-1}. and the analysis regions in this work was considered according to the frequencies at which the characteristic peaks of MWCNTs appear. These regions are: 1100-1800 cm^{-1} at which D, G^+, and G^-− bands are visible, 2000-3000 cm^{-1} to see the G'− band. The range that exceeds the capacity of the grid was made to do not cut the peak that appeared at the boundaries. The spectrums of MWCNTs was taken in a wider range without divisions (50-4000 cm^{-1}), but they will be presented in the same regions that the other samples. Since the sample was prepared in glass slides instead of silicon wafers (it will be described later), it is not possible to calibrate the spectrum with the well reported silicon peak at 520 cm^{-1}. In that manner, it was used a neon lamp to calibrate each measurement and the data base of Peak-O-Mat Software as in the work made by Michaelian[93]. In both Rama types of equipment, the wavelength of the laser was 532 nm, a flat-correction for all measurements (except MWCNTs pristine) was performed to avoid fluorescence of Kaol, and the calibration was made using a Neon lamp and the database of Peak-o-Mat software. The grid used was 600*lines/mm*, 50× optical e objective lens, the hole aperture was 65, the scanning and acquisition times were varied in each sample.

Table 4.2: Raman measurements parameters in the region 1100-1800 cm^{-1} and 2000-3000 cm^{-1} of Kaol pristine, MWCNTs pristine, and Kaolinite/MWCNT nanocomposites (Kaol-MW nanocomposites) at different wt. % of MWCNTs

Sample	Equipment	Grid (*lines/mm*)	Scan time (*s*)	Acquisition time (*s*)	Objective lens	Hole aperture
Kaol pris	*R. HR Evolution*	600	13	30	50×	65
MWCNTs pris	*R. Aramis*	600	5	5	50×	65
Kaol-MW-5%	*R. HR Evolution*	600	13	25	50×	65
Kaol-MW-1%	*R. Aramis*	600	13	25	50×	65
Kaol-MW-0.1%	*R. Aramis*	600	13	25	50×	65
Kaol-MW-0.05%	*R. HR Evolution*	600	10	25	50×	65

SEM measurements was performed in *FEI HELIOS NanoLab 600* equipment. In order to reduce the accumulation

of charge in the sample, it was used silver paint in the SEM pin stub and a little amount of the dried nanocopmposites from the glass slide was used for SEM measurements. The samples were dried in a vacuum oven at 80°C for 24 hours. Four samples were prepared for SEM measurements: Kaol pristine, MWCNTs pristine, Kaol-MW-5% and Kaol-MW-1% due to the availability of the equipment. The voltage, the dwell time (time that data from the channel detector are being logged while the electron beam is at a single pixel position.), and the horizontal field width (HFW) parameters are summarized in Table 4.3 for each sample.

Table 4.3: SEM measurement parameters for Kaol pristine, MWCNTs pristine, Kaol-MW-5% and Kaol-MW-1%

Sample	Voltage (kV)	Dwell time (ns)	Horizontal Field Width (HFW) (μm)
Kaol pris	5	50	138
MWCNTs pris	5	50	13.8
Kaol-MW-5%	10	100	1.73 5
Kaol-MW-1%	10	100	1.04

Chapter 5

Results & Discussion

In this chapter, Raman and Scanning Electron Microscopy (SEM) results are presented. It contains the details of the data treatment such as the software and function used to fit the data. Besides, tables of tendencies of nanocomposites when the amount of Carbon Nanotubes (CNTs) varies are presented and the corresponding analysis of the obtained data.

5.1   Raman Spectroscopy[*]

The Raman measurements was performed as it was mentioned in the Chapter 4 section 4.2, and the spectrums were analyzed with Peak-fit software. The fitting of the Kaolinite clay (Kaol) bands was made with Gauss×Lorentz shapes based in the analysis presented by Frost and Kristof[53]. The peaks of Multiwalled Carbon Nanotubes (MWCNTs) was fit with Breit-Wigner-Fanos (BWFs) shape for the D, G^+, G^-, sp^3 hybridization (new) bands, for the G' and $G + D$ bands the Voight Amp shape was used, and Lorentz shape was employed for amorphous carbon (new peak). The origin of the new features mentioned will be explained later. In Fig. 5.1 it is shown the Raman spectrum with the experimental and fit data of the pristine samples and the nanocomposites of Kaol and MWCNTs. From top to bottom, a) is the spectrum of Kaol pristine, b) is the MWCNTs pristine, c) is the Kaol-MW-5% nanocomposites, d) is the Kaol-MW-1% nanocomposites, e) is the Kaol-MW-0.1% nanocomposites, and f) is the Kaol-MW-0.05% nanocomposites. In the left site it is plotted the $1100 - 1800 cm^{-1}$ range in which the $D - band$, G^+ and G^- bands of CNTs appears and in the right side is plotted the $2000 - 3000 cm^{-1}$ where $2D$ or G' bands appear. The red dots correspond to the calibrated experimental data, the filled curves belongs to the deconvoluted fit showing each contribution to the final fit plot which is presented with continuous black lines. Gauss×Lorentz, BWF, Lorentz, and Voig Amp shapes are showed with a filling of black, blue, green, and cyan color respectively. The MWCNTs Raman spectrum pristine showed five bands: the D band at $1339 cm^{-1}$, the G^- band at $1595 cm^{-1}$, the G^+ band at $1595 cm^{-1}$, the G' band at $2670 cm^{-1}$ and the overtone $G + D$ at $2918 cm^{-1}$.
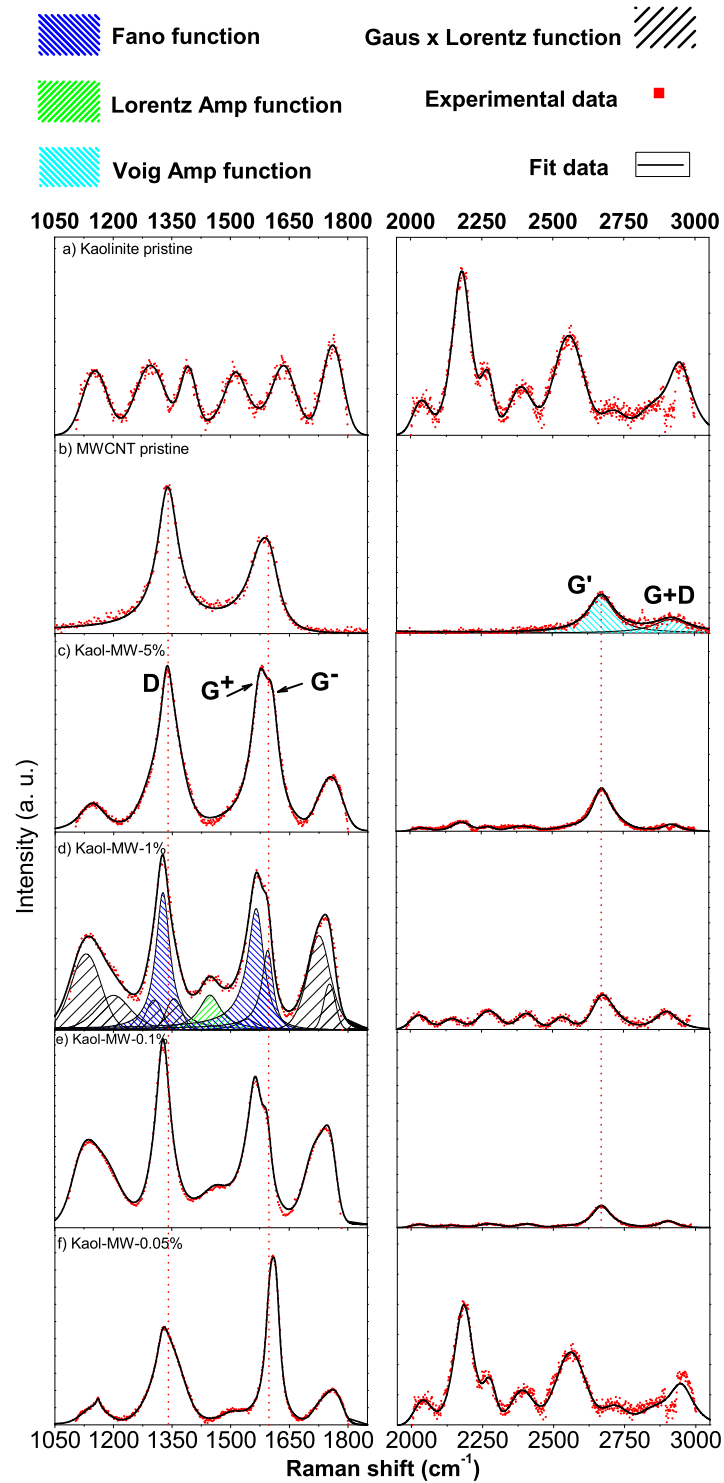
Figure 5.1: Raman spectrum region of D, G^+, G^- (left), and G' (right) line of MWCNTs a) Kaol pristine b) MWCNTs pristine c) Kaol-MW-5% d) Kaol-MW-1% e) Kaol-MW-0.1% f) Kaol-MW-0.05%

Table 5.1: Raman features in cm^{-1} for different weight percentage of MWCNTs in Kaol nanocomposites

Raman band	Sample					Possible origin
	Pristine	5 wt.%	1 wt.%	0.1 wt.%	0.05 wt.%	
D	1339.14	1337.00	1326.49	1327.00	1326,54	Assigned to defects in the lattice [15,41]
amorphous carbon	–	–	1446.91	1459.14	1502.32	Assigned to amorphous carbon [94]
G_{ta-C}	–	–	1542.00	1542.00	1598.20	Asociated with sp^3 hybridaton [94]
G_{2ta-C}	–	–	–	–	1160	Asociated with high concentration of sp^3 hybridaton [94]
G^+	1570.00	1573.46	1565.06	1562.42	1605.00	In plane vibration along the tube axis of Γ point [15,41]
G^-	1595.00	1605.78	1594.79	1592.09	1615.48	In plane vibration transversely to the axis tube of Γ point (inner tubes) [15,41]
G'	2670.36	2669.83	2670.36	2668.00	–	Double resonance process and an overtone of D band [15,41]

The information enclosed in the G^- band of CNTs tells about charge transfer, doping, and functionalization[2,41,43,95]. The doping in carbon nanotubes affects differently in the C-C bonds along the tube axis and in the bonds along the radial direction. Depending of the concentration of doping the nanotubes could exhibit either a lattice contraction or expansion[78]. We expected to see a trend of shift in the G^- band of the MWCNTs nanocomposites as a function of the wt.% concentration of nanotubes. However, in our results, the G^- line suffer an upshift, downshift, downshift and upshift in the Kaol-MW-5%, Kaol-MW-1%, Kaol-MW-0.1%, and Kaol-MW-0.05% respectively as it is showed in the Fig.5.2, it also shows the error bars in the points where the software produced the standard error of the fitting which serves as a reference of how well are our data fitted. In Fig. 5.1 the red dot lines were plotted at the frequency of the principal bands of MWCNTs pristine: D, G^-, and G' bands. It serves as reference to observe the shifts in the nanocomposites. These results have to be explained in parallel with the asymetry factor of the BWF function used to fit the G^- band which are tabulated in the Table 5.2. From the configuration of the software the values close to one means that the BWF function is symmetric. When phonons are coupled to the continuum excitation spectra of the free electrons, the Raman peak exhibits the so called BWF line-shape[80]. Kaol-MW-5% presented an upshift of 10 cm^{-1} and BWF line-shape with an asymetry factor of 0.84 which means that it has free available electrons that goes from the the π orbitals of CNTs to the kaolinite which acts as an electron acceptor[1]. It corresponds to a p-type doping and an effective stiffening of the C-C bonds is produced by this electron transfer which is reflected confirmed with the upshift of the G^- band[78]. Also, the electron transfer produces holes in the MWCNTs structure which moves down the Fermi level in energy. It provokes that less energy (high frequency) being required to excite electrons[1]. Consequently, a change in the Raman signals has sense because the technique is sensible to Fermi level changes.
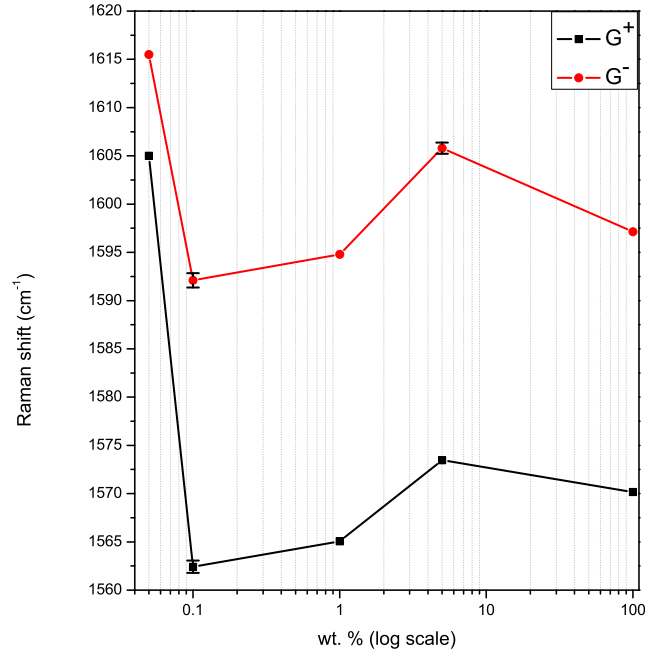
Figure 5.2: Frequency at which G^+ and G^- Raman bands appear of Kaolinite/MWCNT nanocomposites (Kaol-MW nanocomposites) with different weight percentage concentrations of MWCNTs in a logarithmic scale for the x axis that correspond to the weight percentage concentration of MWCNTs. 100 wt.% represents the pristine MWCNTs

Table 5.2: Asymmetry factor of the fit function of the G^- band in the MWCNTs pristine and Kaol-MW nanocomposites. The values far to one implies higher asymetry and therefore metallic behavior

Sample	Asymmetry factor
Pristine MWCNTs	0.74
Kaol-MW-5%	0.84
Kaol-MW-1%	1.00
Kaol-MW-0,%	1.00
Kaol-MW-0,05%	1.00

The nanocomposites with 1 wt. % and 0.1 wt. % MWCNTs concentration showed an downshift and no free

elecron avilable given by the asymetry factor (1.00). Also, the sownshift was just one and two wavenumbers respectively. The G^- band appeared almost at the same frequency that the pristine MWCNTs. In this case, electrons from Kaol are promoted to the π^* orbital of the MWCNTs resulting in a slow $n-$ type doping[1]. The Fermi level in these cases suffers a movement up in energy allowing the coupling between the free carries and the phonons requiring less more energy (lower frequency) to excite electrons[78]. The nanocomposites with he lowest concentration of MWCNTs showed an asymmetry factor of one which implies that there is not available free electrons, but the electron transfer was from MWCNTs to Kaol resulting in a p-type doping[1]. The upshift in this case despite the lack of free electrons was attributed to a high formation of sp^3 hybridization[75].

Table 5.3: Full Width at Half Maximun (FWHM) of MWCNTs pristine, and Kaol-MW nanocomposites at different MWCNTs wt. % concentration.

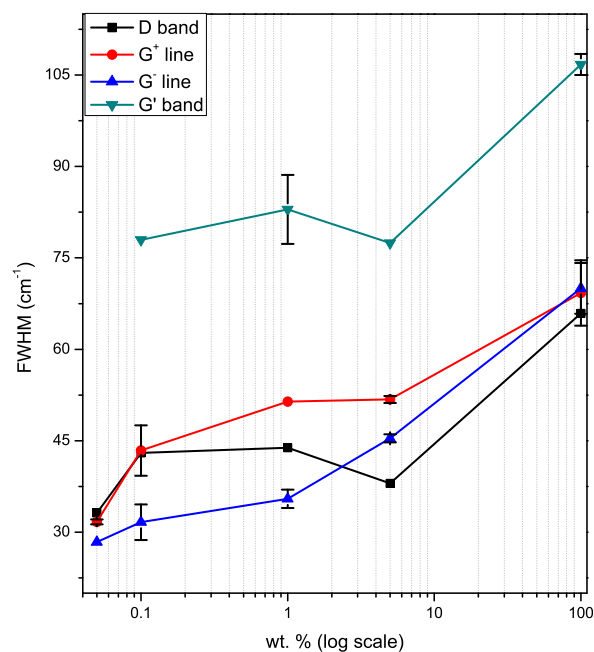| Raman feature	FWHM (cm^{-1})				
	Pristine MWCNTs	5 wt.%	1 wt.%	0.1 wt.%	0.05 wt.%
D band	65.91	38.00	43.84	43.00	33.15
amorphous carbon	–	–	67.25	92.58	67.25
G_{ta-C}	–	–	55.57	67.69	23.73
G^+ band	69.24	51.77	41.93	43.39	31.68
G^- band	69.99	45.38	35.46	31.63	28.39
G' band	110.70	77.44	82.94	77.95	–

Figure 5.3: FWHM of D, G^+, G^-, and G' Kaol-MW nanocomposites bands.

The attachment of Kaol to the sidewall MWCNTs should produce a break down of the translational symmetry[78]. The disorder is observed in the intensity of the D band, but a more accurate value for the disorder is the I_D/I_{G^-} ratio[45]. The ratio of the G band and D band depends on both the degree of graphitization and the alignment of graphite planes and is an indicator of the quality of CNTs[80,96]. The quality of the samples will be better when the I_D/I_{G^-} ratio is lower[2]. In Table 5.4 it is tabulated the I_D/I_{G^-} ratio for the pristine MWCNTs and the kaol-MW nanocomposites, and in Fig. 5.4 it is shown the tendency of the I_D/I_{G^-} ratio where the value of 100 corresponds to the MWCNTs pristine. It also contains the error bars calculated with the propagation error theory using the standard errors obtained from the fitting data. This value was high for the MWCNTs pristine which implies that the received MWCNTs contained a lot of defects. The I_D/I_{G^-} ratio for Kaol-MW-5% decreases until 0.87 suggesting that the process of preparation of the nanocomposites reduces the defects. Maitra *et al.*[96] reported that in the preparation on their composites nanofibers the I_G/I_D ratio (the inverse of the I_D/I_{G^-} ratio) increased upon increasing the concentration of CNTs.

In our results, the Kaol-MW-5% nanocomposites presented a lower I_D/I_{G^-} ratio (0.87) with respect to the pristine that was 2.00 (see Fig. 5.4 and Table 5.4). This behavior is associated with the literature to the graphitization and the alignment of graphite planes, quality of the CNTs in general as it was mentioned. Thus, this nanocomposites

suffered an increase in their quality with respect to the pristine MWCNTs associated with the sonication process and the amount of MWCNTs presents in the nanocomposites. The Kaol-MW-1% and Kaol-MW-0.1% presented an increase in the I_D/I_{G^-} ratio compared to the Kaol-MW-5% nanocomposites suggesting the increase of defects. In this case, it was associated with the formation of sp^3 hybridization from sp^2 bonds[97]. The intensity of the D band increases when there are more sp^3 bonds[97] and therefore the I_D/I_{G^-} ratio increases. Kaol-MW-0.05% presented the lowest I_D/I_{G^-} ratio which implies a higher-ordered structure. In this case, the structure presents more sp^3 bonds and it began to stabilize itself and to have fewer deffects[75].
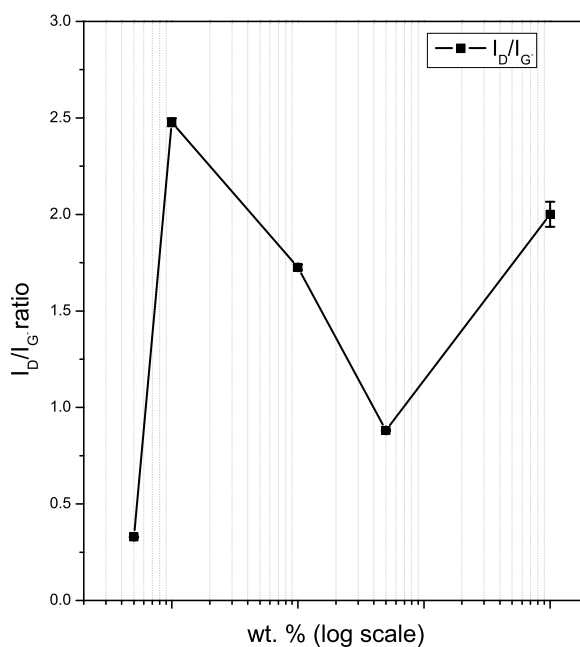

Figure 5.4: I_D/I_{G^-} ratio for Kaol-MW nanocomposites, the pristine MWCNTs are represented by 100 wt.% in a log scale

This value increased for the Kaol-MW-1% and Kaol-MW-0.1% until 1.72 and 2.47 respectively. The defects decreased in the Kaol-MW-1%, but it increased in the Kaol-MW-0.1% nanocomposites. The FWHM of the D band als is a measurement of the quality of the MWCNTs. This value had a similar tendency that I_D/I_{G^-} ratio, high for MWCNTs pristine (65.91 cm^{-1}), lower in the Kaol-MW-5% nanocomposites (38 cm^{-1}), an increase in the Kaol-MW-1% and Kaol-MW-0.1% nanocomposites (43.84 cm^{-1} and 43 cm^{-1} respectively), and the lowest in the Kaol-MW-0.05% (33.15 cm^{-1}). Finally, in the Kaol-MW-0.05% nanocomposites the D' band disappeared, it has

been reported that intensity ratio of the G' and G bands, $I_{G'}/I_{G^-}$ ratio, decreased by the Fermi level shift due to the influence of electronâelectron. Also, it has been reported a decrease in the $I_{G'}/I_{G^-}$ ratio in doped Single-walled Carbon Nanotubes (SWCNTs)[98]. In Fig. 5.5 it is shown the $I_{G'}/I_{G^-}$ ratio of the pristine MWCNTs and the Kaol-MW nanocomposites, and the values was tabulated in Table 5.4. There was a tendency to decrease in the $I_{G'}/I_{G^-}$ ratio, with the highest value of MWCNTs (0.52). It decreased until 0,39, 0,37, and 0,33 in the Kaol-MW-5%, Kaol-MW-1%, and Kaol-MW-0.1% nanocomposites respectively. Smaller values of FWHM indicates higher degree of crystallinity[99]. The $I_{G'}/I_{G^-}$ ratio in the Kaol-MW-0.05% nanocomposites was zero because the G' band disappeared. It suggested the highest doping in the nanocomposites with the lowest concentration of MWCNTs[98].
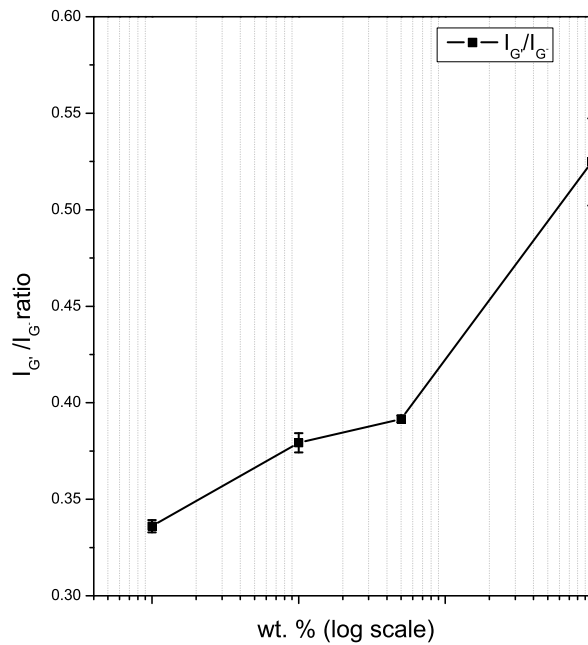

Figure 5.5: $I_{G'}/I_{G^-}$ ratio for Kaol-MW nanocomposites. The pristine MWCNTs are represented by 100 wt.% in a log scale

Table 5.4: I_D/I_{G^-} ratio and $I_{G'}/I_{G^-}$ ratio of MWCNTs and Kao-MW nanocomposites which gives information about quality and doping respectively. Values close to zero in the I_D/I_{G^-} ratio are related to high quality of MWCNTs, and values close to zero in the $I_{G'}/I_{G^-}$ ratio refers to high doping levels[98]

Sample	I_D/I_{G^-} ratio (cm^{-1})	$I_{G'}/I_{G^-}$ ratio (cm^{-1})
Pristine MWCNTs	2.00	0.52
Kaol-MW-5%	0.87	0.39
Kaol-MW-1%	1.72	0.37
Kaol-MW-0,1%	2.47	0.33
Kaol-MW-0,05%	0.32	–

Additionally to the characteristic peaks of MWCNTs, two new peaks appeared in the Raman spectrum of all the nanocomposites except in the Kaol-MW-5%. In Table 5.1 are tabulated the frequencies at which these new peaks appeared. The first new peak was attributed to amorphous carbon and it appeared at 1446.91 cm^{-1}, 1459 cm^{-1}, and 1502.32 cm^{-1} in the Kaol-MW-1%, Kaol-MW-0.1%, and Kaol-MW-0.05% nanocomposites respectively. The second new peak appeared at 1542 cm^{-1} in the Kaol-MW-1%, and Kaol-MW-0.1% nanocomposites, and at 1595.20 cm^{-1} in the Kaol-MW-0.05% nanocomposites. This peak was assigned to a sp^3 hybridization. The peak that corresponds to the sp^3 hybridization was not obvious. This peak was included to enhance the data fit, without this peak the experimental data of G^- and G^+ band base did not match with enough accuracy with the fit functions. It is suggested a phase transformation in the nanocomposites with the variation of MWCNTs concentration.

Ferrari and Robertson[94] proposed three-stage phase transformation: (a) from graphite to nanocrystalline graphite, (b) from nanocrystalline graphite to amorphous carbon (a-C), and (c) a-C to tetrahedral carbon t$_{a-C}$. They indicated that first stage is characterized by the movement of the G band from 1581 cm^{-1} to ≈ 1602 cm^{-1}, an increase in the I_D/I_{G^-} ratio, and there is not dispersion of the G mode. In the second stage the G band decreased from 1600 cm^{-1} to ≈ 1581 cm^{-1}, the I_D/I_{G^-} ratio tends to zero, and the dispersion of the G band increased. The last stage the content of sp^3 raises from $10-20\%$ to $\approx 85\%$, the G peak increased from ≈ 1510 cm^{-1} to ≈ 1570 cm^{-1}, the I_D/I_{G^-} ratio tends to zero, and the dispersion of the G mode occurred[94]. In that manner, the received MWCNTs presented the G^- band around 1595 cm^{-1} and a I_D/I_{G^-} ratio of 2.0 which has similar characteristic to the first stage phase transformation which makes sense because we used MWCNTs that is the equivalent to nanocrystals. The important fact is that the pristine presented a lot of defects. The I_D/I_{G^-} ratio, the position of the G^- band, the peak of amorphous carbon of the Kaol-MW nanocompoposites, and all the other facts mentioned before could be interpreted in the following mechanism:

The MWCNTs pristine may be related to the first-stage phase formation because the nanotubes are the equivalent of the nanocrystalline graphite, and the position of the G^- band appeared at 1595 cm^{-1}. It presented a metallic behavior and a lot of defects which was observed in the I_D/I_{G^-} ratio which could be the activated factor to functionalization in the nanocomposites with Kaol. The Kaol-MW-5% nanocomposites did not presented the peak of amorphous carbon neither the peak of sp^3 hybridization, but the I_D/I_{G^-} ratio decreased and the FWHM decreased which suggested that in these nanocomposites the quality of MWCNTs enhanced. There was interactions between MWCNTs and Kaol

which was confirmed by the charge transfer shown in the shift of the G^- band, and the metallic behavior disappeared. The Kaol-MW-1% and Kaol-MW-0.1% nanocomposites presented charge transfer and sp^3 hybridization, charge transfer, no metallic behavior, and formation of amorphous carbon. The quality is better in the Kaol-MW-1% which presented a lower I_D/I_{G^-} ratio and lower FWHM of the D band. In the Kaol-MW-0.1% nanocomposites, there was more modifications in the structure of MWCNTs. Finally, the Kaol-MW-0.05% nanocomposites achieved the best quality in terms of the I_D/I_{G^-} ratio and the FWHM of the D band[2,96]. Also, it presented charge transfer and the peaks of sp^3 hybridization[75]. These facts located the Kaol-MW-0.05% nanocomposites in the third-stage phase formation with high sp^3 hybridization content. Moreover, just in the Kaol-MW-0.05% nanocomposites appeared a third new peak at 1160 cm^{-1} which confirms the highest concentration of sp^3 hybridization.

5.2 Scanning Electron Microscopy*

To portrait the surface morphology of the composite system, and to calculate the particle size of the samples it was performed SEM images for the pristine samples, and the nanocomposites of Kaol and MWCNTs: Kaol-MW-5% and Kaol-MW-1% which are showed in Fig. 5.6. A flake of Kaol pristine appeared in the Fig. 5.6a with a grain size of 0.06 mm. This image presented an artifact in the top of the Kaol grain known as scan line shifts produced from positioning errors of the scanning electron beam[100]. Also, there are some bright regions which was produced because the sample accumulated the electrons that hit the sample. It is recommended to coated the sample with a conductor material like carbon or gold to avoid the accumulation of charge in the sample. The Fig 5.6b corresponds to the pristine MWCNTs. The image showed a boundle of MWCNTs where the nanotubes are interacting between them via Van der Waals forces which remain them together. There are a small region with charge accumulation which is caused by the orientation of the sample. In the edges o samples could occur more accumulation of charge, and it could be fixed rotating the sample until the bright regions disappeared as much it is possible. Also, the voltage used in the pristine samples were lower the the voltage in the nanocompoites. This reduction of voltage also allowed to decrease the accumulation of charge. In Fig. 5.6c it is shown the SEM image of the Kaol-MW-5% nanocomposites. In this image, the nanotubes appeared dispersed around the Kaol with some particles attached to the nanotubes. Kaol-MW-1% is shown in Fig. 5.6d, it also showed the nanotubes dispersed and with some particles attached to it. The voltage applied in the Kaol-MW nanocomposites was higher than the pristine samples, and it was not shown more areas of charge accumulation. In some way, the nanocomposites are interacting to produce this effect. Finally, in Fig. 5.6e it is showed an statistical analysis of MWCNTs diameter obtained from the SEM image of Kaol-MW-1% carried out with 40 measurements which shows that the diameter of the MWCNTs is between 15 and 22 nm.

These images showed how the MWCNTs are physically distributed in the clay matrix. Fig. 5.6d shows how the MWCNTs are placed between the flakes of the Kaol, and their are more spread than the pristine MWCNTs. It is possible to appreciate some small grains of Kaol adhered to MWCNTs. Furthermore, it confirms the interaction between the MWCNTs and MWCNTs that the Raman measurements showed. Our samples that correspond to Fig. 5.6d is the nanocomposites that we expected to obtain.

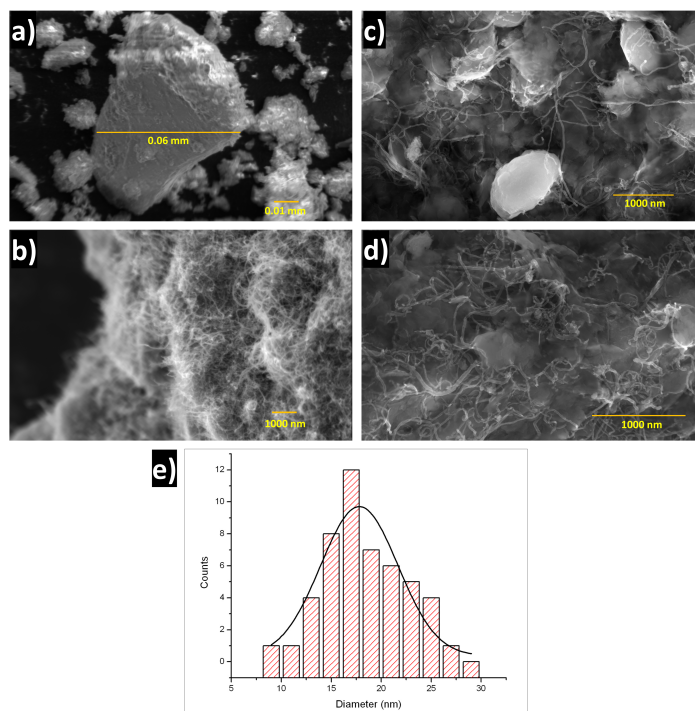*The measurements was carried out with the support of ZMP

Figure 5.6: SEM images of a) a flake of Kaol pristine that presented a grain size of 0.06 mm, b) MWCNTs pristine, c) Kaol-MW-5% nanocomposites, d) Kaol-MW-1% nanocomposites, and e) statistical analysis of MWCNTs diameter of Kaol-MW-1% nanoccomposites

Chapter 6

Conclusions & Outlook

In this work, it was successfully made nanocomposites of Kaolinite clay (Kaol) and Multiwalled Carbon Nanotubes (MWCNTs) at four different wt. % concentration of MWCNTs: 5 wt. %, 1 wt. %, 0.1 wt. %, and 0.05 wt. %. These nanocomposites were characterized by Raman spectroscopy and Scanning Electron Microscopy (SEM), and analysis of of doping, crystallinity, quality, charge transfer, and functionalization was made in base of the fit function used, the frequency of the peaks, the Full Width at Half Maximun (FWHM), the I_D/I_{G^-} ratio, the $I_{G'}/I_{G^-}$ ratio, and the appearance of two new peaks associated to amorphous carbon and sp^3 hybridization. Finally, all the described features were related with the work made by Ferrari and Robertson [94]. In their work, it is described three-stage phase transformation: (a) from graphite to nanocrystalline graphite, (b) from nanocrystalline graphite to amorphous carbon (a-C), and (c) from a-C to tetrahedral carbon t_{a-C}.

We found that the nanocomposites with the highest and lowest concentration that corresponds to 5wt.% and 0.05 wt.% presented an upshift of the G^- band. It corresponds a $p-$ type doping in which electrons from the π orbitals are promoted to the Kaolinite which acted as an electron acceptor, and it created holes carriers in the Carbon Nanotubes (CNTs). The nanocomposites made of Kaol and 1%wt. and 0.1%wt. of MWCNTs concentration presented a downshift of the G^- band. In this case, electrons from Kaol are promoted to the π^* orbital of the MWCNTs resulting in a $n-$ type doping. The crystallinity analysis via FWHM of the G^- band and the quality obtained from the I_D/I_{G^-} ratio showed that the Kaol-MW-0.05% nanocomposites had the best crystallinity and the best quality.

Two new peaks appeared in all the nanocomposites, except in the Kaol-MW-5% nanocomposites. In the Kaol-MW-5% nanocomposites there was an enhancement of the quality attributed to the sonication process. These peaks where attributed to the formation of amorphous carbon and the sp^3 hybridization. Finally, the analysis of the $I_{G'}/I_{G^-}$ ratio was used to known the degree of formation of sp^3 hybridization. This value showed a decrease tendency when the concentration of MWCNTs decreased. These facts located the Kaol-MW-0.05% nanocomposites in the third-stage phase formation with high sp^3 hybridization content. Moreover, just in the Kaol-MW-0.05% nanocomposites appeared a third new peak at $1160 cm^{-1}$ which confirms the highest concentration of sp^3 hybridization.

This research can be used as a base for the analysis of more nanocomposites based on Kaol and CNTs. In this

work it was not showed the region where the OH group of Kaol appears, a wide range of measurement could help to understand better the mechanism of functionalization. In the same way, Fourier Transform Infrared Microscopys (FTIRs) measurements are suggested as well as X-ray Diffraction (XRD) characterization. Additional information could be obtained using Single-walled Carbon Nanotubes (SWCNTs) or any other type of CNTs to analyze the functionalization with modified CNTs.

Bibliography

[1] Souza Filho, A.; Jorio, A.; Samsonidze, G. G.; Dresselhaus, G.; Saito, R.; Dresselhaus, M. Raman spectroscopy for probing chemically/physically induced phenomena in carbon nanotubes. *Nanotechnology* **2003**, *14*, 1130.

[2] Anwar, A. W. Investigation of doping and photoexcitation in carbon nanotubes using Raman spectroscopy. Ph.D. thesis, Université de Toulouse, Université Toulouse III-Paul Sabatier, 2011.

[3] Wesley, L. In *Clays and clay minerals: Geological Origin, mechanical properties and industrial applications*; Wesley, L., Ed.; Nova Science, 2014.

[4] Benco, L.; Tunega, D.; Hafner, J.; Lischka, H. Upper Limit of the O- H⋯O Hydrogen Bond. Ab Initio Study of the Kaolinite Structure. *The Journal of Physical Chemistry B* **2001**, *105*, 10812–10817.

[5] Murray, H. H. Overview- clay mineral applications. *Applied Clay Science* **1991**, *5*, 379–395.

[6] Adams, F. C.; Barbante, C. Nanoscience, nanotechnology and spectrometry. *Spectrochimica Acta Part B: Atomic Spectroscopy* **2013**, *86*, 3–13.

[7] Vance, M. E.; Kuiken, T.; Vejerano, E. P.; McGinnis, S. P.; Hochella Jr, M. F.; Rejeski, D.; Hull, M. S. Nanotechnology in the real world: Redeveloping the nanomaterial consumer products inventory. *Beilstein journal of nanotechnology* **2015**, *6*, 1769–1780.

[8] Okpala, C. C. Nanocomposites–an overview. *Int. J. Eng. Res. Dev* **2013**, *8*, 17.

[9] Ates, M.; Eker, A. A.; Eker, B. Carbon nanotube-based nanocomposites and their applications. *Journal of adhesion science and Technology* **2017**, *31*, 1977–1997.

[10] Grobert, N. Carbon nanotubes–becoming clean. *Materials today* **2007**, *10*, 28–35.

[11] Iijima, S. Carbon nanotubes: past, present, and future. *Physica B: Condensed Matter* **2002**, *323*, 1–5.

[12] Price, G. J.; Nawaz, M.; Yasin, T.; Bibi, S. Sonochemical modification of carbon nanotubes for enhanced nanocomposite performance. *Ultrasonics sonochemistry* **2018**, *40*, 123–130.

[13] Andrews, R.; Jacques, D.; Qian, D.; Rantell, T. Multiwall carbon nanotubes: synthesis and application. *Accounts of chemical research* **2002**, *35*, 1008–1017.

[14] Karthik, P.; Himaja, A.; Singh, S. P. Carbon-allotropes: synthesis methods, applications and future perspectives. *Carbonlett* **2014**, *15*, 219–237.

[15] Belin, T.; Epron, F. Characterization methods of carbon nanotubes: a review. *Materials Science and Engineering: B* **2005**, *119*, 105–118.

[16] Iijima, S.; Brabec, C.; Maiti, A.; Bernholc, J. Structural flexibility of carbon nanotubes. *The Journal of chemical physics* **1996**, *104*, 2089–2092.

[17] Patakfalvi, R.; Oszko, A.; DeKany, I. Synthesis and characterization of silver nanoparticle/kaolinite composites. *Colloids and Surfaces A: Physicochemical and Engineering Aspects* **2003**, *220*, 45–54.

[18] Czarnecka, A. Preparation and characterization of kaolinite-based nanocomposite materials. Ph.D. thesis, Université d'Ottawa/University of Ottawa, 2013.

[19] Gupta, V. *Surface charge features of kaolinite particles and their interactions*; The University of Utah, 2011.

[20] Chen, B.; Evans, J. R.; Greenwell, H. C.; Boulet, P.; Coveney, P. V.; Bowden, A. A.; Whiting, A. A critical appraisal of polymer–clay nanocomposites. *Chemical Society Reviews* **2008**, *37*, 568–594.

[21] Li, X.; Peng, K.; Chen, H.; Wang, Z. TiO 2 nanoparticles assembled on kaolinites with different morphologies for efficient photocatalytic performance. *Scientific reports* **2018**, *8*, 11663.

[22] Hajjaji, W.; Kovičová, A.; Pullar, R.; Tobaldi, D.; Lopez-Galindo, A.; Jammousi, F.; Rocha, F.; Labrincha, J. Effective removal of anionic and cationic dyes by kaolinite and TiO$_2$/kaolinite composites. *Clay Minerals* **2016**, *51*, 19–27.

[23] Camargo, P. H. C.; Satyanarayana, K. G.; Wypych, F. Nanocomposites: synthesis, structure, properties and new application opportunities. *Materials Research* **2009**, *12*, 1–39.

[24] Baksi, S.; Biswas, S. Nanocomposites–An Overview. *The Scitech Journal* **2014**, *1*, 22–30.

[25] Ajayan, P. M.; Schadler, L. S.; Braun, P. V. *Nanocomposite science and technology*; John Wiley & Sons, 2006.

[26] AZoNano, Nanocomposites- An Overview of Properties, Applications and Definition. 2019; `https://www.azonano.com/article.aspx?ArticleID=1832`.

[27] Song, S. H. The effect of clay/multiwall carbon nanotube hybrid fillers on the properties of elastomer nanocomposites. *International Journal of Polymer Science* **2018**, *2018*.

[28] Sedaghat, S. Synthesis of clay-CNTs nanocomposite. *Journal of Nanostructure in Chemistry* **2013**, *3*, 24.

[29] Simari, C.; Potsi, G.; Policicchio, A.; Perrotta, I.; Nicotera, I. Clay–carbon nanotubes hybrid materials for nanocomposite membranes: advantages of branched structure for proton transport under low humidity conditions in PEMFCs. *The Journal of Physical Chemistry C* **2016**, *120*, 2574–2584.

[30] Mohammadi, T.; Tofighy, M. A.; Pak, A. Synthesis of carbon nanotubes on macroporous kaolin substrate via a new simple CVD method. *International Journal of Chemical Reactor Engineering* **2009**, *7*.

[31] Herrero-Latorre, C.; Álvarez-Méndez, J.; Barciela-García, J.; García-Martín, S.; Peña-Crecente, R. Characterization of carbon nanotubes and analytical methods for their determination in environmental and biological samples: A review. *Analytica chimica acta* **2015**, *853*, 77–94.

[32] Medjo, R. E. *Physical and Chemical Properties of Carbon Nanotubes*; IntechOpen, 2013.

[33] Laserna, J. J. An introduction to Raman spectroscopy: introduction and basic principles. *Raman/Infrared Spectroscopy* **2014**,

[34] Yadav, V. B.; Gadi, R.; Kalra, S. Synthesis and characterization of novel nanocomposite by using kaolinite and carbon nanotubes. *Applied Clay Science* **2018**, *155*, 30–36.

[35] Hirsch, A. The era of carbon allotropes. *Nature materials* **2010**, *9*, 868.

[36] McEnaney, B. Structure and bonding in carbon materials. *Carbon materials for advanced technologies* **1999**, 1–34.

[37] Peschel, G. Carbon-carbon bonds: hybridization. *Obtained online from: http://www. physik. fu-berlin. de/einrichtungen/ag/ag-reich/lehre/Archiv/ss2011/docs/Gina_Peschel-Handout. pdf, published on* **2011**, *5*.

[38] Pan, L. S.; Kania, D. R. *Diamond: electronic properties and applications*; Springer Science & Business Media, 2013.

[39] Pisanty, A. The electronic structure of graphite: A chemist's introduction to band theory. *Journal of Chemical Education* **1991**, *68*, 804.

[40] Kang, J.; Shin, D.; Bae, S.; Hong, B. H. Graphene transfer: key for applications. *Nanoscale* **2012**, *4*, 5527–5537.

[41] Dresselhaus, M. S.; Dresselhaus, G.; Saito, R.; Jorio, A. Raman spectroscopy of carbon nanotubes. *Physics reports* **2005**, *409*, 47–99.

[42] Pierson, H. O. *Handbook of carbon, graphite, diamonds and fullerenes: processing, properties and applications*; William Andrew, 2012.

[43] Dresselhaus, M.; Eklund, P. Phonons in carbon nanotubes. *Advances in Physics* **2000**, *49*, 705–814.

[44] Dresselhaus, M. S.; Jorio, A.; Hofmann, M.; Dresselhaus, G.; Saito, R. Perspectives on carbon nanotubes and graphene Raman spectroscopy. *Nano letters* **2010**, *10*, 751–758.

[45] Lokota, M. Characterizing exfoliated multiwall carbon nanotubes by Scanning Electron Microscopy and Raman Spectroscopy. M.Sc. thesis, Freie Universität Berlin, 2016.

[46] Dervishi, E.; Li, Z.; Xu, Y.; Saini, V.; Biris, A. R.; Lupu, D.; Biris, A. S. Carbon nanotubes: synthesis, properties, and applications. *Particulate Science and Technology* **2009**, *27*, 107–125.

[47] Yamashita, S. Nonlinear optics in carbon nanotube, graphene, and related 2D materials. *APL Photonics* **2019**, *4*, 034301.

[48] LLC, N. Properties of MWCNT. 2015; `https://www.nanoshel.com/properties-of-mwcnt`.

[49] Thomsen, C.; Reich, S. *Light Scattering in Solid IX*; Springer, 2006; pp 115–234.

[50] Neto, J. C.; Kimura, S. P. R.; Adeodato, M. G.; Neto, J. E.; do Nascimento, N. R.; Ferrareso, L. M. Intercalation and exfoliation mechanism of kaolinite during the emulsion polymerization. *Chemical Engineering Transactions* **2017**, *57*, 1453–1458.

[51] Elimat, Z.; Zihlif, A.; Ragosta, G. Optical and thermal properties of polycarbonate/kaolinite composites. *Journal of Thermoplastic Composite Materials* **2010**, *23*, 793–805.

[52] Sempeho, S. I.; Kim, H. T.; Mubofu, E.; Pogrebnoi, A.; Shao, G.; Hilonga, A. Encapsulated urea-Kaolinite Nanocomposite for controlled release fertilizer formulations. *Journal of Chemistry* **2015**, *2015*.

[53] Frost, R. L.; Kristof, J. *Clay surfaces: fundamental and applications*; Elsevier, 2004; pp 184–215.

[54] Han, Z.; Zhang, F.; Lin, D.; Xing, B. Clay minerals affect the stability of surfactant-facilitated carbon nanotube suspensions. *Environmental science & technology* **2008**, *42*, 6869–6875.

[55] Pastorková, K.; Jesenák, K.; Kadlečíková, M.; Breza, J.; Kolmačka, M.; Čaplovičová, M.; Lazišťan, F.; Michalka, M. The growth of multi-walled carbon nanotubes on natural clay minerals (kaolinite, nontronite and sepiolite). *Applied Surface Science* **2012**, *258*, 2661–2666.

[56] Shaban, M.; Hassouna, M. E.; Nasief, F. M.; AbuKhadra, M. R. Adsorption properties of kaolinite-based nanocomposites for Fe and Mn pollutants from aqueous solutions and raw ground water: kinetics and equilibrium studies. *Environmental Science and Pollution Research* **2017**, *24*, 22954–22966.

[57] Kumari, R.; Singh, F.; Yadav, B. S.; Kotnala, R. K.; Peta, K. R.; Tyagi, P. K.; Kumar, S.; Puri, N. K. Ion irradiation-induced, localized sp^2 to sp^3 hybridized carbon transformation in walls of multiwalled carbon nanotubes. *Nuclear Instruments and Methods in Physics Research Section B: Beam Interactions with Materials and Atoms* **2017**, *412*, 115–122.

[58] Graves, P.; Gardiner, D. Practical raman spectroscopy. *Springer* **1989**,

[59] Smith, E.; Dent, G. *Modern Raman spectroscopy: a practical approach*; Wiley, 2019.

[60] Leeds, S. M. Characterisation of the gas-phase environment in a microwave plasma enhanced diamond chemical vapour deposition reactor using molecular beam mass spectrometry. Ph.D. thesis, University of Bristol, 1999.

[61] Keresztury, G. R aman Spectroscopy: Theory. *Handbook of vibrational spectroscopy* **2006**,

[62] Bumbrah, G. S.; Sharma, R. M. Raman spectroscopy–Basic principle, instrumentation and selected applications for the characterization of drugs of abuse. *Egyptian Journal of Forensic Sciences* **2016**, *6*, 209–215.

[63] Potcoava, M. C.; Futia, G. L.; Aughenbaugh, J.; Schlaepfer, I. R.; Gibson, E. A. Raman and coherent anti-Stokes Raman scattering microscopy studies of changes in lipid content and composition in hormone-treated breast and prostate cancer cells. *Journal of Biomedical Optics* **2014**, *19*, 111605.

[64] Umbach,; Hines, *Raman Spectroscopy*.

[65] Rosa, A. L. Raman Spectroscopy Basics. 2011; `http://web.pdx.edu/~larosaa/Applied_Optics_464-564/Projects_Optics/Raman_Spectrocopy/Raman_Spectroscopy_Basics_PRINCETON-INSTRUMENTS.pdf`.

[66] Karlen, S. Fabrication and characterization of MEMS alkali vapor cells used in chip-scale atomic clocks and other atomic devices. Ph.D. thesis, Université de Neuchâtel, 2018.

[67] Hotokka, M. *Molecular spectroscopy*; 2013.

[68] Panici, K. Raman Spectrosopy. **2004**,

[69] McCreery, R. L. *Raman spectroscopy for chemical analysis*; John Wiley & Sons, 2005; Vol. 225.

[70] LaPlant, F. *Emerging Raman Applications and Techniques in Biomedical and Pharmaceutical Fields*; Springer, 2010; pp 1–24.

[71] Erdogan, T.; Mizrahi, V. Thin-film filters for Raman spectroscopy. *Spectroscopy* **2004**, *19*, 113–116.

[72] Filter Types for Raman Spectroscopy Applications. `https://www.ahf.de/pdfs/Technical-Note_Filter_Types_for_Raman_Spectroscopy_by_Semrock.pdf`.

[73] Wang, S. Modern Techniques for Food Authentication. 2009.

[74] Adar, F. Considerations of Grating Selection in Optimizing a Raman Spectrography. *Spectroscopy* **2013**, *28*.

[75] Ferraro, J. R. *Introductory raman spectroscopy*; Elsevier, 2003.

[76] Dubessy, J.; Caumon, M.; Rull, F.; Sharma, S. Instrumentation in Raman Spectroscopy: Elementary Theory and Practice. 2012.

[77] Bokobza, L.; Zhang, J. Raman spectroscopic characterization of multiwall carbon nanotubes and of composites. *Express Polymer Letters* **2012**, *6*.

[78] Terrones, M.; Souza Filho, A. G.; Rao, A. M. *Carbon nanotubes*; Springer, 2007; pp 531–566.

[79] Zdrojek, M.; Gebicki, W.; Jastrzebski, C.; Melin, T.; Huczko, A. Studies of multiwall carbon nanotubes using Raman spectroscopy and atomic force microscopy. 2004.

[80] Saito, R.; Hofmann, M.; Dresselhaus, G.; Jorio, A.; Dresselhaus, M. Raman spectroscopy of graphene and carbon nanotubes. *Advances in Physics* **2011**, *60*, 413–550.

[81] Siregar, S. Double resonance Raman spectra of G0 and G bands of graphene. M.Sc. thesis, Department of Physics Graduate School of Science Tohoku University, 2015.

[82] Mahajan, S.; Bambole, M.; Gokhale, S.; Gaikwad, A. Monitoring structural defects and crystallinity of carbon nanotubes in thin films. *Pramana* **2010**, *74*, 447–455.

[83] Aharinejad, S.; Lametschwandtner, A. *Microvascular Corrosion Casting in Scanning Electron Microscopy*; Springer, 1992; pp 44–51.

[84] Zhou, W.; Wang, Z. L. *Scanning microscopy for nanotechnology: techniques and applications*; Springer science & business media, 2007.

[85] Technology, J. S. A. Scanning electron microscopy A to Z: Basic Knowledge for Using the SEM. `https://www.jeol.co.jp/en/applications/pdf/sm/sem_atoz_all.pdf`.

[86] Smallman, R. E. *Modern physical metallurgy*; Elsevier, 2016.

[87] Fuchs, F. J. *Ultrasonic cleaning: fundamental theory and application*; 1995.

[88] Yan, L.; Zhang, C.; Xu, Z. Highly effective delamination of kaolinite and emergence of a novel nanoclub-like crystal. *Journal of Wuhan University of Technology-Mater. Sci. Ed.* **2008**, *23*, 566–570.

[89] Pérez-Maqueda, L. A.; Franco, F.; Pérez-Rodríguez, J. L. Comparative study of the sonication effect on the thermal behaviour of 1: 1 and 2: 1 aluminium phyllosilicate clays. *Journal of the European Ceramic Society* **2005**, *25*, 1463–1470.

[90] Yang, K.; Yi, Z.; Jing, Q.; Yue, R.; Jiang, W.; Lin, D. Sonication-assisted dispersion of carbon nanotubes in aqueous solutions of the anionic surfactant SDBS: The role of sonication energy. *Chinese science bulletin* **2013**, *58*, 2082–2090.

[91] Johansson, Ö.; Pamidi, T.; Khoshkhoo, M.; Sandström, Å. *Sustainable and energy efficient leaching of tungsten (W) by ultrasound controlled cavitation*; Luleå tekniska universitet, 2017.

[92] Jagadish, K.; Srikantaswamy, S.; Byrappa, K.; Shruthi, L.; Abhilash, M. R. Dispersion of multiwall carbon nanotubes in organic solvents through hydrothermal supercritical condition. *Journal of Nanomaterials* **2015**, *16*, 320.

[93] Michaelian, K. The Raman spectrum of kaolinite# 9 at 21 C. *Canadian Journal of Chemistry* **1986**, *64*, 285–294.

[94] Ferrari, A. C.; Robertson, J. Interpretation of Raman spectra of disordered and amorphous carbon. *Physical review B* **2000**, *61*, 14095.

[95] Yang, Q.-H.; Hou, P.-X.; Unno, M.; Yamauchi, S.; Saito, R.; Kyotani, T. Dual Raman features of double coaxial carbon nanotubes with N-doped and B-doped multiwalls. *Nano letters* **2005**, *5*, 2465–2469.

[96] Maitra, T.; Sharma, S.; Srivastava, A.; Cho, Y.-K.; Madou, M.; Sharma, A. Improved graphitization and electrical conductivity of suspended carbon nanofibers derived from carbon nanotube/polyacrylonitrile composites by directed electrospinning. *Carbon* **2012**, *50*, 1753–1761.

[97] Alshamsi, H. What does decrease in Id/Ig value in raman spectroscopy indicate for carbon based compounds? 2017; `https://www.researchgate.net/post/What_does_decrease_in_Id_Ig_value_in_raman_spectroscopy_indicate_for_carbon_based_compounds`.

[98] Suzuki, S.; Hibino, H. Characterization of doped single-wall carbon nanotubes by Raman spectroscopy. *Carbon* **2011**, *49*, 2264–2272.

[99] Benoit, J.; Buisson, J.; Chauvet, O.; Godon, C.; Lefrant, S. Low-frequency Raman studies of multiwalled carbon nanotubes: experiments and theory. *Physical Review B* **2002**, *66*, 073417.

[100] Maraghechi, S.; Hoefnagels, J. P.; Peerlings, R. H.; Geers, M. G. Correction of scan line shift artifacts in scanning electron microscopy: An extended digital image correlation framework. *Ultramicroscopy* **2018**, *187*, 144–163.

Abbreviations

BET Brunauer-Emmett-Teller 14
BSE Back-Scattered Electron 22, 24
BWF Breit-Wigner-Fano 21, 33, 35

CNT Carbon Nanotube xvii, 1–5, 7–11, 14, 15, 18–21, 24, 27, 29, 33, 35, 38, 45, 46

DMF Dimethylformamide 14
DOS Density of States xvii, 9

EDS Energy-Dispersive X-rays Microscopy 15

FBZ First Brillouin Zone 6, 21
FTIR Fourier Transform Infrared Microscopy 14, 46
FWHM Full Width at Half Maximun xvii, xix, 21, 37–42, 45

HFW Horizontal Field Width 32
HTEM High Resolution Transmision Electron Microscopy 14, 15

Kaol Kaolinite clay xvii, xix, 2, 4, 5, 12–15, 24, 27, 29–35, 37, 38, 41, 43–46
Kaol-MW nanocomposites Kaolinite/MWCNT nanocomposites xiii, xvii, xix, 31, 36–38, 43

MWCNT Multiwalled Carbon Nanotube xiii, xvii, xix, 2–4, 7, 8, 10, 11, 14, 15, 18, 19, 21, 27, 29–45

NNI National Nanotechnology Initiative 1

RBM Radial Breathing Mode 18, 20, 21

SAED Selected Area Electron Diffraction 15
SE Secondary Electron 23, 24
SEM Scanning Electron Microscopy xi, xiii, xvii, xix, 3, 4, 14, 15, 22–24, 27, 29, 31–33, 43–45
SWCNT Single-walled Carbon Nanotube 2, 7, 8, 10, 20, 21, 40, 46

TEM Transmission Electron Microscopy 15

XRD X-ray Diffraction 14, 15, 46
XRP X-ray Photoelectron Spectroscopy 15

ZMP Zentralinstitut für neue Materialien und Prozesstechnik iii, iv, ix, 29, 33, 43